Article

RZZ-Spindly and CENP-E form an integrated platform to recruit dynein to the kinetochore corona

Verena Cmentowski[1,2,*] ID, Giuseppe Ciossani[1,†] ID, Ennio d'Amico[1,‡] ID, Sabine Wohlgemuth[1], Mikito Owa[3], Brian Dynlacht[3] & Andrea Musacchio[1,2,**] ID

Abstract

Chromosome biorientation on the mitotic spindle is prerequisite to errorless genome inheritance. CENP-E (kinesin-7) and dynein–dynactin (DD), microtubule motors with opposite polarity, promote biorientation from the kinetochore corona, a polymeric structure whose assembly requires MPS1 kinase. The corona's building block consists of ROD, Zwilch, ZW10, and the DD adaptor Spindly (RZZS). How CENP-E and DD are scaffolded and mutually coordinated in the corona remains unclear. Here, we show that when corona assembly is prevented through MPS1 inhibition, CENP-E is absolutely required to retain RZZS at kinetochores. An RZZS phospho-mimetic mutant bypasses this requirement, demonstrating the existence of a second receptor for polymeric RZZS. With active MPS1, CENP-E is dispensable for corona expansion, but strictly required for physiological kinetochore accumulation of DD. Thus, we identify the corona as an integrated scaffold where CENP-E kinesin controls DD kinetochore loading for coordinated bidirectional transport of chromosome cargo.

Introduction

As points of attachment of chromosomes to spindle microtubules in mitosis and meiosis, kinetochores are pivotal for chromosome segregation and genome inheritance (Cheeseman & Desai, 2008; Musacchio & Desai, 2017). Kinetochores are layered structures built on specialized chromosome loci named centromeres (Fig 1A). A centromere–proximal complex assembled on centromere landmarks and consisting of 16 subunits in humans (the constitutive centromere associated network or CCAN) recruits a centromere-distal layer involved in microtubule binding, the KMN network (Cheeseman & Desai, 2008). The KMN network forms from three constituent subcomplexes, the Knl1 complex (Knl1C, two subunits), the Mis12 complex (Mis12C, four subunits), and the Ndc80 complex (Ndc80C, four subunits). The Mis12C is a scaffold required for coordinated recruitment of the Knl1C and the Ndc80C (Cheeseman & Desai, 2008; Musacchio & Desai, 2017). Ndc80C is a microtubule receptor that promotes mature, "end-on" interaction observed during metaphase, when spindle microtubules orient perpendicularly to the outer kinetochore (Cheeseman et al, 2006; DeLuca et al, 2006). Ndc80C and Knl1C also represent distinct but interconnected branches of an outer kinetochore regulatory network that controls biorientation and the timing of mitotic exit, as explained below.

In mitotic prometaphase, before the achievement of end-on binding and biorientation, outer kinetochores of metazoans assemble an outermost dense layer covered by fibrous material and named the kinetochore corona (Kops & Gassmann, 2020) (Fig 1A and B). The building block of the corona is a complex of the ROD-Zwilch-ZW10 (RZZ) complex with Spindly, a dynein–dynactin (DD) adaptor (Mosalaganti et al, 2017; Pereira et al, 2018; Sacristan et al, 2018; Raisch et al, 2022). MPS1, a protein kinase with various regulatory functions at mitotic kinetochores, phosphorylates ROD on two N-terminal residues to promote the polymerization of RZZ-Spindly (RZZS) that assembles the corona (Rodriguez-Rodriguez et al, 2018; Raisch et al, 2022).

Two microtubule motors with opposite polarity facilitate chromosome alignment in prometaphase from the kinetochore corona by transporting chromosomes as cargoes while walking along the microtubule lattice. One is the homo-dimeric plus-end-directed kinesin-7 centromere protein E (CENP-E, 2701 residues in humans) (Yen et al, 1991, 1992). Like other kinesins, CENP-E is autoinhibited, likely through an interaction of its N- and C-terminal regions

1 Department of Mechanistic Cell Biology, Max Planck Institute of Molecular Physiology, Dortmund, Germany
2 Centre for Medical Biotechnology, Faculty of Biology, University Duisburg-Essen, Essen, Germany
3 Department of Pathology, New York University Cancer Institute, New York University School of Medicine, New York, NY, USA
  *Corresponding author. Tel: +49 231 133 2101; E-mail: verena.cmentowski@mpi-dortmund.mpg.de
  **Corresponding author. Tel: +49 231 133 2101; E-mail: andrea.musacchio@mpi-dortmund.mpg.de
  †Present address: European Institute of Oncology, Milan, Italy
  ‡Present address: Division of Structural Studies, MRC Laboratory of Molecular Biology, Cambridge, UK

Figure 1.

◀

Figure 1. CENP-E^{2070C} contains binding sites for BUBR1 and RZZS.

A Organization of the human kinetochore and corona.

B Drawing depicting the hierarchical organization of outer kinetochore and kinetochore corona components. Thick arrows indicate the recruitment of a protein to the protein indicated by the arrowhead. Thin arrows indicate phosphorylation. The white arrow indicates polymerization.

C Representative images of the localization of CENP-E after depletion of Zwilch and BUBR1 in HeLa cells. Zwilch RNAi treatment was performed with 100 nM siRNA for 72 h. Following 48 h after Zwilch RNAi treatment cells were transfected with 100 nM BUBR1 siRNA. Following 8 h after transfection, cells were synchronized in the G2 phase with 9 μM RO3306 for 15 h and then released into mitosis. Subsequently, cells were immediately treated with 3.3 μM Nocodazole, 10 μM MG132 for an additional hour. CENP-C was used to visualize kinetochores and DAPI to stain DNA. Three biological replicates were performed. Scale bar: 5 μm.

D Quantification of CENP-E levels at kinetochores of the experiment shown in panel C. *n* refers to individually measured kinetochores.

E Organization of CENP-E with coiled-coil prediction.

F Representative images showing the localization of different ^{EGFP}CENP-E constructs in prometaphase after depletion of CENP-E with 60 nM siRNA. 13 h after RNAi treatment HeLa cells were electroporated with electroporation buffer or recombinant ^{EGFP}CENP-E constructs as indicated. Following an 8 h recovery, cells were synchronized in the G2 phase with 9 μM RO3306 for 15 h and then released into mitosis. Subsequently, cells were immediately treated with 3.3 μM Nocodazole for an additional hour. CENP-C was used to visualize kinetochores and DAPI to stain DNA. Three biological replicates were performed. Scale bar: 5 μm.

G Quantification of EGFP levels at kinetochores of the experiment shown in panel F. *n* refers to individually measured kinetochores.

H ^{mCH}RZZ^{mCh}S ring-binding assays showing the recruitment of various ^{EGFP}CENP-E truncations (10 nM concentration) to ^{mCH}RZZ^{mCh}S rings (approximately 40 nM concentration). The experiment was performed once. Scale bar: 5 μm.

I RZZS ring-binding assays showing the recruitment of ^{EGFP}CENP-E^{2070C} to ^{mCH}RZZ^{mCh}S rings is unaffected by increasing concentrations of BUBR1^{KD}. The experiment was performed once. Scale bar: 5 μm.

Data information: Statistical analysis (in D and G) was performed with a nonparametric *t*-test comparing the two unpaired groups (Mann–Whitney test). Symbols indicate: ****$P \leq 0.0001$. Red bars represent the median and interquartile range.

that is regulated by Aurora kinase phosphorylation (Espeut *et al*, 2008; Kim *et al*, 2008, 2010; Vitre *et al*, 2014; Craske *et al*, 2022; Eibes *et al*, 2023). How CENP-E autoinhibition regulates end-on attachment, however, remains unclear.

The other motor in the kinetochore corona is the minus-end-directed dynein (Pfarr *et al*, 1990; Gassmann, 2023), a 1.4 MDa complex composed of two copies each of six distinct polypeptides (Carter *et al*, 2016; Reck-Peterson *et al*, 2018). On its own, dynein is poorly motile. Its motility is greatly enhanced by dynactin, a 1.1 MDa 23-subunit assembly built from 11 distinct polypeptides. The interaction of dynein and dynactin is reinforced by specialized activating adaptor molecules (Carter *et al*, 2016; Reck-Peterson *et al*, 2018). Activating adaptors are extended, dimeric coiled-coil proteins characterized by a set of conserved motifs that promote the stabilization of the DD complex (Carter *et al*, 2016; Reck-Peterson *et al*, 2018; Olenick & Holzbaur, 2019). While conserved in their outline, adaptors respond to different stimuli in different subcellular locales and interact with different cargoes. Spindly is recognized as the kinetochore adaptor for DD (Griffis *et al*, 2007; Yamamoto *et al*, 2008; Chan *et al*, 2009; Gassmann, 2023). Its localization to kinetochores requires an interaction with the RZZ complex that is greatly enhanced by Spindly farnesylation (Kops & Gassmann, 2020; Gassmann, 2023).

In addition to promoting biorientation, the corona has also been shown to promote microtubule nucleation (Wu *et al*, 2023) and to contribute to the spindle assembly checkpoint (SAC), a pathway that delays anaphase onset until successful biorientation of all sister chromatid pairs (Lara-Gonzalez *et al*, 2021; Fischer, 2022). One of the main components of the SAC, the MAD1:MAD2 core complex, is also a constituent of the corona, where it also interacts with the CDK1:Cyclin B complex (Hoffman *et al*, 2001; Alfonso-Perez *et al*, 2019; Allan *et al*, 2020; Jackman *et al*, 2020). SAC signaling at each kinetochore subsides during the conversion of kinetochore attachments from the microtubule lattice to the microtubule end (Magidson *et al*, 2015; Kuhn & Dumont, 2017, 2019; Sacristan *et al*, 2018; Chakraborty *et al*, 2019). Following this lateral to the end-on conversion of kinetochore-microtubule attachment, which involves CENP-E (Chakraborty *et al*, 2019), the corona is rapidly

disassembled (shedding or stripping) (Hoffman *et al*, 2001; Wojcik *et al*, 2001; Basto *et al*, 2004). Shedding is caused by activation of retrograde dynein motility and promotes removal of corona components and their relocation to the spindle poles. This process also removes MAD1:MAD2 from the kinetochore, leading to suppression of SAC signaling (Fava *et al*, 2011; Maldonado & Kapoor, 2011; Ballister *et al*, 2014; Kuhn & Dumont, 2017, 2019).

Correct coordination of end-on attachment and checkpoint silencing through shedding is crucial for mitosis. The precise order of molecular events behind this coordination, however, remains unclear. Whether CENP-E is merely recruited to the kinetochore corona as an outermost terminal component or rather contributes to the stabilization of the corona and the localization and function of other proteins, most notably DD, is currently unknown. Thus, dissecting the interactions of CENP-E at the corona has become pressing. MAD1 has been proposed to act as a kinetochore receptor for CENP-E (Akera *et al*, 2015). Other studies, however, did not identify a role of MAD1 in CENP-E recruitment (Sharp-Baker & Chen, 2001; Martin-Lluesma *et al*, 2002). Binding to CENP-E has also been proposed to control activation of the kinase activity of BUBR1 in SAC control (Mao *et al*, 2003, 2005), but other studies have suggested BUBR1 is a pseudokinase devoid of catalytic activity (Suijkerbuijk *et al*, 2012; Breit *et al*, 2015). BUBR1 interacts directly with CENP-E and contributes to its kinetochore recruitment (Ciossani *et al*, 2018; Legal *et al*, 2020). We and others, however, observed that depletion of BUBR1 causes only modest reduction of CENP-E from prometaphase kinetochores (Lampson & Kapoor, 2005; Akera *et al*, 2015; Ciossani *et al*, 2018). Furthermore, unlike CENP-E, BUBR1 does not expand into the corona, suggesting that at least another prominent CENP-E receptor must be present in the corona.

A second set of pressing questions concerns the RZZS and its role in corona assembly. The recent realization that RZZS is the building block of the corona (Mosalaganti *et al*, 2017; Pereira *et al*, 2018; Sacristan *et al*, 2018; Raisch *et al*, 2022) raises questions on how the RZZS becomes recruited to kinetochores. For instance, it is unknown whether the requirements for kinetochore localization of the individual RZZS building blocks and of their polymer are the same. Furthermore, MPS1 kinase activity regulates corona

expansion, but it is unclear whether it also regulates the interaction of RZZS with the kinetochore, as possibly implied by the reduced kinetochore levels of RZZS upon MPS1 inhibition (Rodriguez-Rodriguez *et al*, 2018). Both the Ndc80C and the Knl1C have been implicated in RZZS recruitment (Lin *et al*, 2006; Chan *et al*, 2009; Pagliuca *et al*, 2009; Sundin *et al*, 2011; Varma *et al*, 2013; Caldas *et al*, 2015; Pereira *et al*, 2018), but other reports also identified these proteins as being at least partly dispensable (Varma *et al*, 2013; Silio *et al*, 2015; Pereira *et al*, 2018; Rodriguez-Rodriguez *et al*, 2018).

Addressing how the kinetochore scaffold influences the corona is very challenging. Each of the two main regulatory branches of the KMN network, the Knl1C and the Ndc80C, individually recruits several regulatory proteins at the same time. These downstream regulators, however, mutually reinforce each other functionally and structurally. For instance, Ndc80C recruits MPS1 (Martin-Lluesma *et al*, 2002; Stucke *et al*, 2004; Hiruma *et al*, 2015; Ji *et al*, 2015), but MPS1 phosphorylates Knl1C to promote recruitment of BUB1, which in turn recruits BUBR1 (Meadows *et al*, 2011; London *et al*, 2012; Yamagishi *et al*, 2012; Primorac *et al*, 2013; Vleugel *et al*, 2013; Krenn *et al*, 2014; Overlack *et al*, 2015). This complex connectivity, which is also expected to influence RZZS and CENP-E recruitment, is an unavoidable source of confusion when simple protein depletions are used as the main perturbation experiment. Therefore, dissecting this complexity necessitates the use of well-characterized separation-of-function mutants (whose identification is usually very laborious) and their re-introduction, possibly in the form of recombinant proteins or protein complexes delivered by protein electroporation (Alex *et al*, 2019; Polley *et al*, 2023) into cells depleted of the endogenous counterpart.

Here we break new ground in our dissection of the kinetochore corona. We demonstrate a direct interaction between CENP-E and the RZZS complex that makes them partly co-dependent for kinetochore localization and function. The interaction promotes the kinetochore recruitment of DD, which is otherwise largely depleted in the absence of CENP-E or in the presence of a CENP-E mutant affecting RZZS binding. While we confirm the importance of BUBR1 in CENP-E recruitment, we find no clear evidence of a role of MAD1. Finally, we show that MPS1 is implicated not only in corona expansion but also in the interaction of RZZS with the kinetochore. We discuss our results also in the context of the regulation of activation of opposing motor activities at different cellular locales.

Results

CENP-E interacts with BUBR1 and RZZS

BUBR1 depletion does not eliminate CENP-E from kinetochores (see Introduction). Because CENP-E localizes to the corona in prometaphase, we asked if perturbations of the corona also affected CENP-E localization. Individual RNAi-based depletions of BUBR1 or Zwilch caused partial reductions of CENP-E in cells arrested in prometaphase with the spindle poison Nocodazole. Co-depletion, on the other hand, caused the extensive reduction of CENP-E at kinetochores (Fig 1C and D). These results imply that both BUBR1 and the RZZS complex promote CENP-E localization. Residual CENP-E observed under conditions of co-depletion may reflect residual

levels of BUBR1 and/or RZZS after the RNAi procedure (Appendix Fig S1A and B), but we cannot exclude a weak interaction with a third receptor (see below).

Next, we tried to identify the kinetochore binding determinants of CENP-E. CENP-E features a C-terminal kinetochore-binding domain encompassing residues 2,126–2,476 (Chan *et al*, 1998) (Fig 1E). In our previous work, we demonstrated that a larger construct encompassing amino acids 2,070–2,701 (hereafter referred to as 2,070C) recapitulates the localization of full-length CENP-E and is sufficient for robust kinetochore localization in prometaphase (Ciossani *et al*, 2018). Indeed, EGFP-CENP-E^{2070C} localized robustly to kinetochores in cells depleted of endogenous CENP-E (Fig 1F and G). This construct also elicited a robust mitotic checkpoint arrest as a consequence of widespread chromosome alignment defects (Appendix Fig S1C and D).

Further dissection of CENP-E^{2070C} in N-terminal (2070–2365) and C-terminal (2366–2701, hereafter referred to as 2366C) fragments revealed that both decorated kinetochores in prometaphase-arrested cells depleted of endogenous CENP-E, even if at partially reduced levels relatively to CENP-E^{2070C} (Fig 1F and G). CENP-E$^{2070–2365}$ localized to kinetochores without apparently extending into the corona. Conversely, CENP-E^{2366C} localized to corona crescents, suggesting that it might interact with RZZS or with another protein associated with the RZZS (Fig 1F and G). Thus, each fragment distinguishes unique determinants of kinetochore localization.

Depletion of BUBR1 prevented the kinetochore recruitment of EGFP-CENP-E$^{2070–2365}$ (the endogenous CENP-E was also depleted to prevent possible confounding effects of dimerization of endogenous and exogenous CENP-E) (Appendix Fig S1E–G). The kinetochore localization of CENP-E$^{2070–2365}$ may be mediated through an interaction with the pseudokinase domain of BUBR1 (Chan *et al*, 1998; Yao *et al*, 2000; Ciossani *et al*, 2018; Legal *et al*, 2020). Indeed, analytical size-exclusion chromatography (SEC) confirmed a direct interaction of CENP-E^{2070C} or CENP-E$^{2070–2365}$, but not CENP-E^{2366C}, with the BUBR1 kinase domain (abbreviated as KD, Appendix Fig S1H and I).

To identify the localization determinants of CENP-E^{2366C}, we asked whether it interacts directly with RZZS. We polymerized mCherry-tagged RZZS *in vitro* to form minicircles, as described (Raisch *et al*, 2022). We then imaged the minicircles by total internal reflection fluorescence (TIRF) microscopy while testing their association with various recombinant EGFP-CENP-E constructs. Both EGFP-CENP-E^{2070C} and EGFP-CENP-E^{2366C} co-localized with the RZZS minicircles *in vitro*, while EGFP-CENP-E$^{2070–2365}$ failed to do so (Fig 1H). The BUBR1 kinase domain also failed to compete with EGFP-CENP-E^{2070C} for co-localization on the RZZS minicircles (Fig 1I). These observations suggest that CENP-E^{2366C} contains a binding site for direct interaction with the RZZS complex. We also used SEC as an alternative methodology to assess the CENP-E-RZZS interaction *in vitro*, but the outcome was inconclusive, as the extended conformation of the isolated binding partners caused them to elute, in isolation or as a putative complex, at essentially identical volumes despite the different molecular mass (V. Cmentowski & A. Musacchio, unpublished results).

Determinants of CENP-E interactions with BUBR1 and RZZS

To dissect further the function of CENP-E$^{2070–2365}$ and CENP-E^{2366C}, we introduced mutations within conserved sequence stretches in

these segments. Specifically, we targeted residues in the segments 2185–2195 and 2492–2507, residing respectively in the BUBR1-binding and RZZS-binding regions of CENP-E (Fig EV1A and B). Analytical SEC confirmed that charge-reversal mutations in the 2185–2195 motif abrogated binding of CENP-E^{2070C} to the pseudokinase domain of BUBR1 (Fig EV1C). Hereafter, we will refer to the mutant in the 2185–2195 region as the BUBR1^{Mut} of CENP-E. Alpha-Fold2 (Jumper *et al*, 2021) predicts this region to be juxtaposed, in the same 4-helix bundle, to residues within the 2310–2320 region whose mutation also abolishes BUBR1 binding (Legal *et al*, 2020) (Fig EV1D).

To test the effects of mutations in the 2492–2507 region, we formed RZZS filaments (Raisch *et al*, 2022) and tested co-localization of EGFP-CENP-E^{2070C}. A mutation of four conserved residues in the 2492–2507 region prevented interaction with RZZS in this assay (Fig EV1E). The binding defect was further substantiated in the TIRF assay, in which we compared binding of EGFP-CENP-E^{2366C} to RZZS minicircles. While the wild type EGFP-CENP-E^{2366C} construct bound minicircles, the mutant did not (Fig EV1F). Hereafter, we will therefore refer to the mutant in the 2492–2507 region as the RZZS^{Mut} of CENP-E.

To test the effects of these mutations on the localization of CENP-E, we generated stable colorectal adenocarcinoma DLD-1 cell lines expressing full-length CENP-E (EGFP-CENP-E^{FL}) or its BUBR1^{Mut} and RZZS^{Mut} mutants (Fig 2A and B). The BUBR1^{Mut} and RZZS^{Mut} localized at kinetochores in Nocodazole treated, prometaphase-arrested cells, with the BUBR1^{Mut} decorating the corona, and the RZZS^{Mut} decorating kinetochores. Conversely, a double mutant was unable to decorate kinetochores, implying that binding to at least one site is necessary for recruitment in prometaphase (Fig 2A and B). Very similar results were obtained

with DLD-1 cell lines expressing the same mutants in the context of EGFP-CENP-E^{2070C} (Fig 2C–E and Appendix Fig S2A) or with purified EGFP-CENP-E^{2070C} protein constructs electroporated in cells (Appendix Fig S2B and C). The BUBR1^{Mut} and RZZS^{Mut} mutations seem to have a more penetrant effect in the context of EGFP-CENP-E^{2070C} than in the context of EGFP-CENP-E^{FL}, possibly because full-length CENP-E has another low-affinity kinetochore binding site that is deleted in CENP-E^{2070C} (compare quantifications in Fig 2B and E). This hypothetical site, however, is unable to promote CENP-E localization when the BUBR1- and RZZS-binding sites of CENP-E are mutated at the same time. Collectively, these results show that the BUBR1 and RZZS binding sites of CENP-E^{2070C} can promote the robust recruitment of CENP-E even independently of each other. Indeed, electroporated EGFP-CENP-E$^{2070–2365}$ and EGFP-CENP-E^{2366C} constructs, respectively, localized to the kinetochore and the corona in cells depleted of endogenous CENP-E. Introducing the BUBR1^{Mut} in EGFP-CENP-E$^{2070–2365}$ or the RZZS^{Mut} in EGFP-CENP-E^{2366C} prevented their kinetochore recruitment (Appendix Fig S2D–G).

In line with the localization experiments, expression of CENP-E^{2070C} had a severe dominant effect on chromosome alignment, likely because the exogenous protein displaces endogenous CENP-E (Fig 2F). The BUBR1^{Mut} (in the context of CENP-E^{2070C}) had less prominent yet very penetrant deleterious effects, whereas the RZZS^{Mut} or the double mutant had a comparatively smaller effect on chromosome alignment, suggesting that they have very limited capacity to displace endogenous CENP-E. These results suggest that integration in the corona (possible for the wild type and BUBR1^{Mut} constructs) is important for the dominant-negative effects of CENP-E^{2070C} on chromosome alignment, and imply that integration in the corona is crucial for the chromosome alignment role of CENP-E.

Figure 2.   Separation of function mutants validate BUBR1 and RZZS as CENP-E partners.

A   Representative images showing the localization of different ^{EGFP}CENP-E^{FL} constructs in stable DLD-1 cell lines arrested in prometaphase. CENP-E RNAi treatment was performed for 24 h with 60 nM siRNA. 8 h after RNAi treatment protein expression was induced through the addition of 10 ng/ml doxycycline and cells were synchronized in the G2 phase with 9 μM RO3306 for 15 h and then released into mitosis. Subsequently, cells were immediately treated with 3.3 μM Nocodazole and 10 ng/ml doxycycline for an additional hour. CENP-C was used to visualize kinetochores and DAPI to stain DNA. Three biological replicates were performed. Scale bar: 5 μm.

B   Quantification of EGFP levels at the kinetochores of the experiment shown in panel A. *n* refers to individually measured kinetochores.

C   Schematic representation of the experimental scheme used for panels D and E.

D   Representative images showing the localization of different ^{EGFP}CENP-E^{2070C} mutants in stable DLD-1 cell lines arrested in prometaphase. CENP-E RNAi treatment was performed for 24 h with 60 nM siRNA. Eight hours after RNAi treatment, protein expression was induced through the addition of 300 ng/ml doxycycline and cells were synchronized in the G2 phase with 9 μM RO3306 for 15 h and then released into mitosis. Subsequently, cells were immediately treated with 3.3 μM Nocodazole and 300 ng/ml doxycycline for an additional hour. CENP-C was used to visualize kinetochores and DAPI to stain DNA. Three biological replicates were performed. Scale bar: 5 μm.

E   Quantification of EGFP levels at the kinetochores of the experiment shown in panel D. *n* refers to individually measured kinetochores.

F   Chromosome alignment analysis of stable DLD-1 cell lines expressing different ^{EGFP}CENP-E^{2070C} constructs. Before fixation, cells were synchronized in the G2 phase with 9 μM RO3306 for 15 h and then released into mitosis. Subsequently, cells were immediately treated with 10 μM MG132 for 2 h. *n* refers to the number of analyzed metaphase cells. Two biological replicates were performed.

G   Schematic representation of the experimental scheme used for panels H and I.

H   Representative images showing the localization of different ^{EGFP}CENP-E^{2070C} mutants in stable DLD-1 cell lines arrested in metaphase. Thirty-two hours after cells were seeded, protein expression was induced through the addition of 300 ng/ml doxycycline and cells were synchronized in the G2 phase with 9 μM RO3306 for 15 h and then released into mitosis. Subsequently, cells were immediately treated with 10 μM MG132 and 300 ng/ml doxycycline for 2 h. CENP-C was used to visualize kinetochores and DAPI to stain DNA. Three biological replicates were performed. Scale bar: 5 μm.

I   Quantification of EGFP levels at kinetochores of the experiment shown in panel H. *n* refers to individually measured kinetochores.

Data information: Statistical analysis in panels B, E, F, and I was performed with a nonparametric *t*-test comparing two unpaired groups (Mann–Whitney test). Symbols indicate: $^{n.s.}P > 0.05$, $*P \leq 0.05$, $**P \leq 0.01$, $****P \leq 0.0001$. Red bars represent the median and interquartile range.
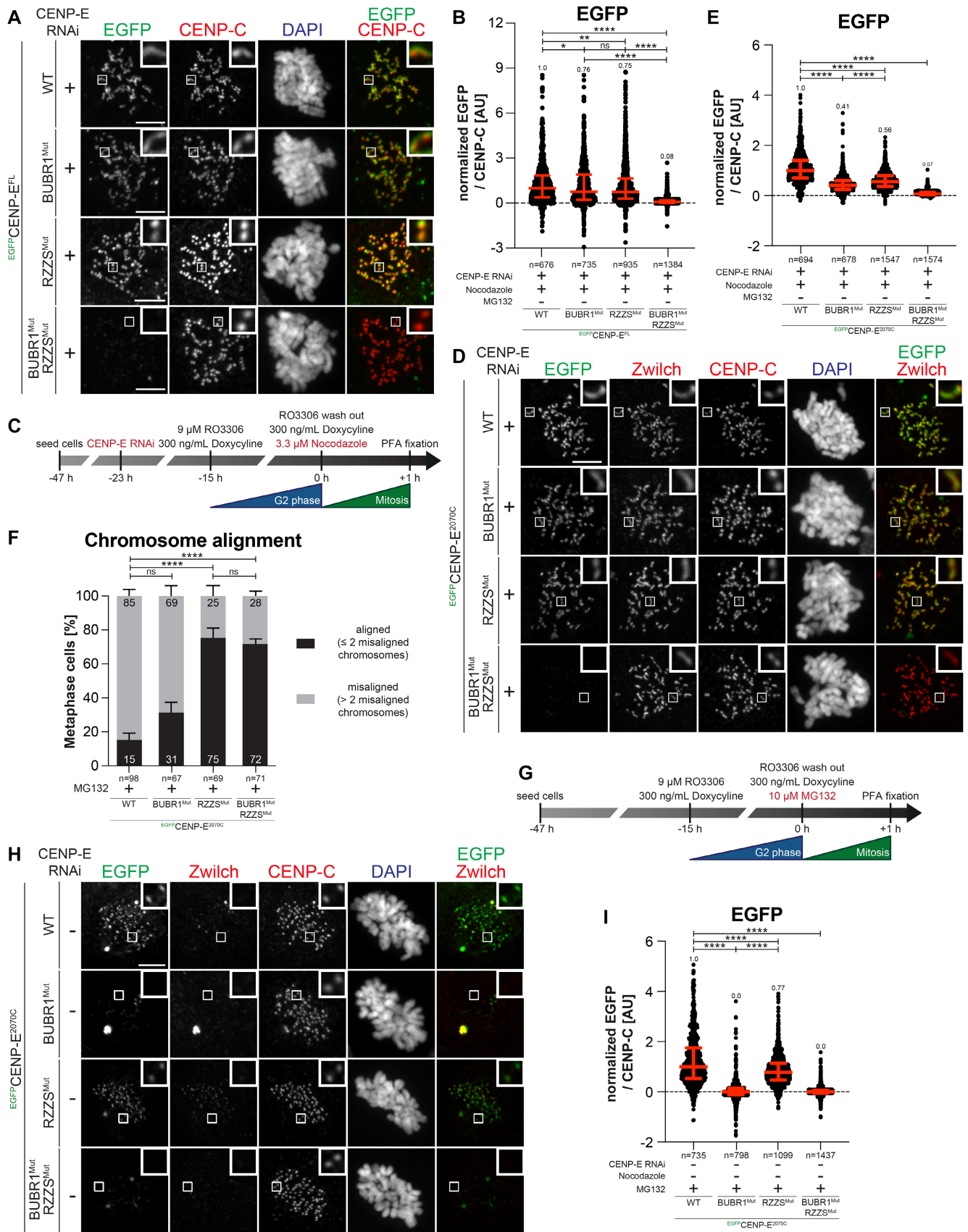
Figure 2.

As previously shown (Gassmann *et al*, 2010), the kinetochore levels of BUBR1 and Zwilch decrease upon bi-orientation; however, while the kinetochore levels of BUBR1 remained comparatively high, Zwilch was only present at trace levels (quantifications shown in Appendix Fig S2H and I). Accordingly, CENP-E was partially retained at kinetochores after corona shedding and achievement of bi-orientation (Ciossani *et al*, 2018). Thus, residual CENP-E on metaphase kinetochores may localize exclusively through BUBR1. Indeed, when localization experiments with BUBR1^{Mut} and RZZS^{Mut} of EGFP-CENP-E^{2070C} were performed in metaphase-arrested cells (through the addition of the proteasome inhibitor MG132), the RZZS^{Mut} decorated kinetochores, whereas the BUBR1^{Mut} was depleted (Fig 2G–I). Also in this case, the double mutant failed to decorate kinetochores. Thus, after corona shedding, BUBR1 is the only residual CENP-E receptor at the kinetochore, so that among the two mutants, only RZZS^{Mut} can retain kinetochore localization in metaphase.

MPS1 inhibition exposes the role of CENP-E in RZZS localization

CENP-E co-localizes with the fibrous corona in prometaphase and is partially removed from the kinetochore upon end-on attachment (Cooke *et al*, 1997; Yao *et al*, 1997; Ciossani *et al*, 2018). Initially, we asked if CENP-E contributes to the kinetochore recruitment or the retention of RZZS in prometaphase-arrested cells. To this end, we used an hTERT-immortalized retinal pigment epithelial-1 (hTERT-RPE-1) cell line in which both endogenous CENP-E alleles were C-terminally tagged with an auxin-inducible degron (AID) and a 3×FLAG tag (Owa & Dynlacht, 2021). In untreated control cells, the resulting CENP-E^{AID} protein adopted the characteristic crescent shape of kinetochore coronas. Addition of the auxin derivative indole acetic acid (IAA) caused rapid degradation of CENP-E^{AID} to undetectable levels within 20 min (Fig 3A) (Owa & Dynlacht, 2021). We then monitored RZZS levels in mitotic cells where CENP-E^{AID}

had been degraded either before or after mitotic entry (respectively indicated as T$_{-30}$ and T$_{+30}$ in Fig 3B–F). Irrespective of the degradation protocol used, these experiments did not reveal large changes in RZZS kinetochore levels upon degradation of CENP-E^{AID} (Fig 3E and F). Similar results were obtained after RNAi-mediated depletion of CENP-E in HeLa cells (Fig EV2A–D). Thus, the kinetochore corona remains stable without CENP-E.

MPS1 kinase phosphorylates ROD on Thr13 and Ser15, and MPS1 inhibition prevents corona expansion while causing only relatively minor reductions of the kinetochore levels of the RZZ complex (Rodriguez-Rodriguez *et al*, 2018; Sacristan *et al*, 2018; Raisch *et al*, 2022). While our observations indicate that CENP-E is not required for RZZS recruitment when corona expansion proceeds normally, CENP-E may contribute to RZZS recruitment before corona expansion. To assess this, we examined RZZS levels after depletion of CENP-E either in the presence of MPS1 kinase activity, or after its inhibition to prevent corona expansion. In agreement with previous reports (Rodriguez-Rodriguez *et al*, 2018; Raisch *et al*, 2022), the specific MPS1 small molecule inhibitor reversine (Santaguida *et al*, 2010) slightly reduced the kinetochore levels of RZZS but effectively prevented corona expansion, as clearly indicated by the dot-like appearance of Zwilch and CENP-E (Fig EV2A–D). RNAi-mediated depletion of CENP-E combined with reversine treatment, however, caused RZZS to disappear from the kinetochore (Fig EV2A–D). To assess the generality of this observation, we synchronized the RPE-1 CENP-E^{AID} line in the G2 phase through the addition of the small molecule RO3306, and added IAA 1 h before release into mitosis to ensure complete degradation of CENP-E^{AID} (Fig 3G). The concomitant depletion of CENP-E^{AID} and inhibition of MPS1 caused RZZS to disappear from the kinetochore, in line with the RNAi experiment (Fig 3H–K).

Recombinant EGFP-CENP-E^{2070C} protein electroporated in HeLa cells depleted of endogenous CENP-E and treated with reversine was sufficient to restore robust RZZS localization (Fig 3L–N).

Figure 3. Combining CENP-E depletion and MPS1 inhibition dissolves the corona.

A   Immunoblot of mitotic RPE-1 cells showing the levels of endogenous CENP-E$^{AID\_3xFLAG}$ treated with 500 μM IAA for the indicated duration. A quantity of 50 μg of cleared lysate was used for each condition, and Tubulin is shown as a loading control. The experiment was performed once.

B   Schematic representation of the cell synchronization protocols for the experiment in panels C–F.

C, D   Representative images showing the effect of degrading CENP-E^{AID} in RPE-1 cells before or after mitotic entry, as shown in panel B. Before fixation, cells were synchronized in the G2 phase with 9 μM RO3306, released into mitosis and immediately treated with 3.3 μM Nocodazole. Cells were treated either 30 min before or 45 min after mitotic entry with 500 μM IAA. CENP-C was used to visualize kinetochores and DAPI to stain DNA. Three biological replicates were performed. Scale bar: 5 μm. The mount is part of a larger experiment in which MAD1 was also visualized (displayed in Fig EV2H; omitted here). Therefore, the images in the CENP-C and DAPI channels are duplicates of those shown in Fig EV2H (where Zwilch was omitted).

E, F   Quantification of kinetochore levels of Zwilch and Spindly in cells depleted of the endogenous CENP-E as shown in panels C and D. *n* refers to individually measured kinetochores.

G   Schematic representation of the cell synchronization protocol for the experiment shown in panels H–K.

H, I   Representative images showing the effects of degrading CENP-E^{AID} in RPE-1 cells before mitotic entry, as shown in panel G. Before fixation, cells were synchronized in the G2 phase with 9 μM RO3306, released into mitosis and immediately treated with 3.3 μM Nocodazole, 10 μM MG132, 500 μM IAA and 500 nM reversine. Three biological replicates were performed. Scale bar: 5 μm.

J, K   Quantification of kinetochore levels of Zwilch and Spindly in cells degraded of the endogenous CENP-E and treated with reversine as shown in panels H and I. *n* refers to individually measured kinetochores.

L   Representative images showing the localization of Zwilch in prometaphase after depletion of CENP-E with 60 nM siRNA. Thirteen hours after RNAi treatment, HeLa cells were electroporated with electroporation buffer or ^{EGFP}CENP-E^{2070C}. Following an 8 h recovery, cells were synchronized in the G2 phase with 9 μM RO3306 for 15 h and then released into mitosis. Subsequently, cells were immediately treated with 3.3 μM Nocodazole, 10 μM MG132 and, where indicated, with 500 nM reversine, for an additional hour. CENP-C was used to visualize kinetochores and DAPI to stain DNA. Three biological replicates were performed. Scale bar: 5 μm.

M, N   Quantification of Zwilch and Spindly levels at kinetochores of the experiment shown in panel L.

Data information: Statistical analysis (panels E, F, J, K, M, and N) was performed with a nonparametric *t*-test comparing two unpaired groups (Mann–Whitney test). Symbols indicate: $^{n.s.}P > 0.05$, $*P \leq 0.05$, $**P \leq 0.01$, $***P \leq 0.001$, $****P \leq 0.0001$. Red bars represent the median and interquartile range.
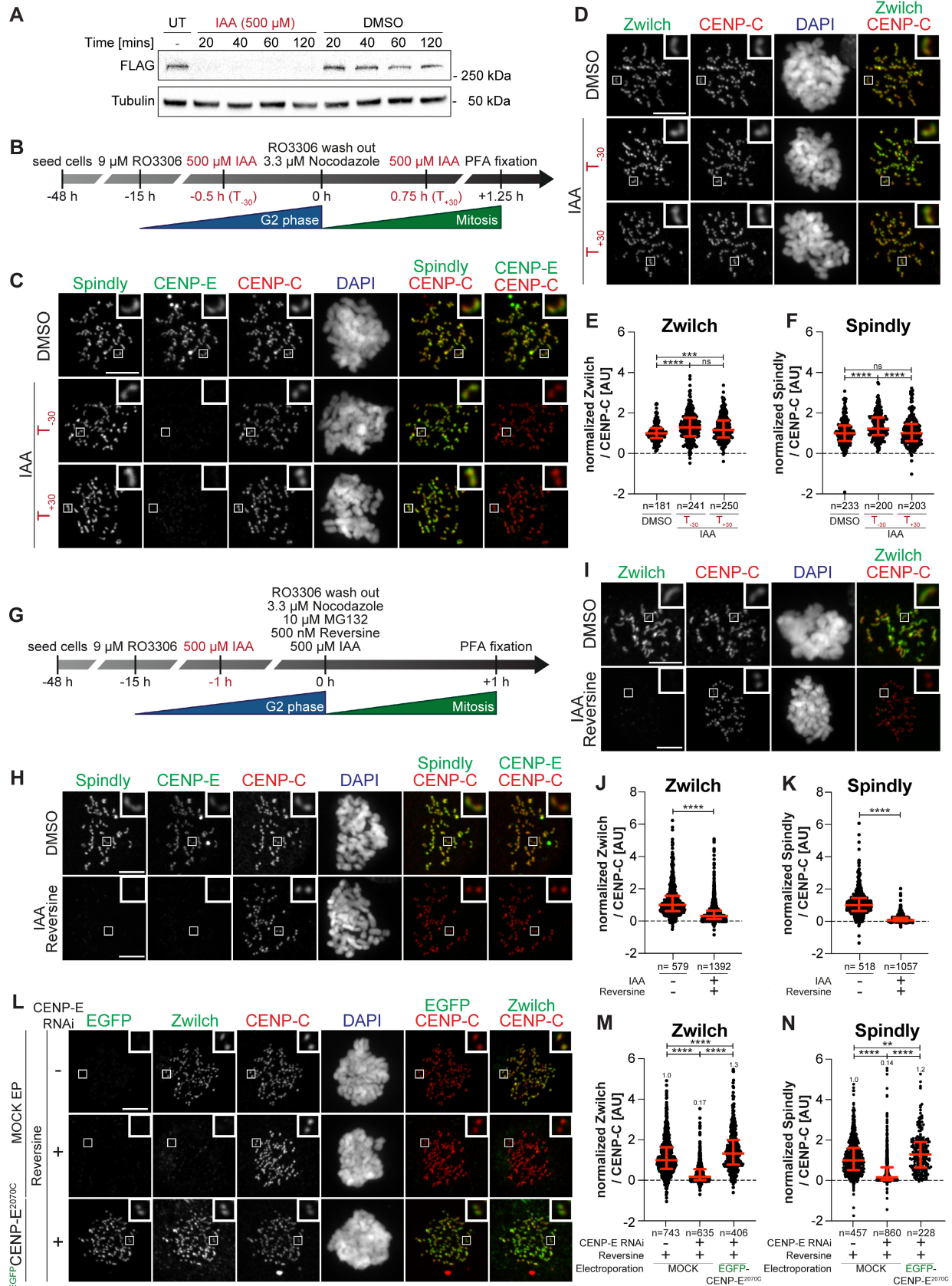
Figure 3.

EGFP-CENP-E^{2366C}, on the other hand, localized normally in the absence of endogenous CENP-E, but further inhibition of MPS1 prevented its kinetochore recruitment and caused a very strong reduction in the kinetochore levels of RZZS (Fig EV2E–G). This result suggests that to be effective in maintaining RZZS at the kinetochore, CENP-E may need to interact at the same time with RZZS and another kinetochore receptor that CENP-E^{2366C} does not recognize, most likely BUBR1. Neither BUBR1^{Mut} nor RZZS^{Mut} (in the context of electroporated CENP-E^{2070C}) localized to the kinetochore in the presence of reversine (Fig EV3A–D). Collectively, these results indicate that CENP-E is dispensable for holding the RZZS onto kinetochores after corona expansion, but is essential for RZZS recruitment when corona assembly is inhibited with an MPS1 inhibitor, a previously unappreciated co-dependence of RZZS and CENP-E for kinetochore recruitment.

IAA-mediated destruction of CENP-E^{AID} in RPE-1 cells did not cause elimination of MAD1, which remained strongly bound to kinetochores (Fig EV2H and I). Treatment with reversine, on the other hand, caused a strong decrease in MAD1 kinetochore levels. No corresponding decrease in the levels of CENP-E was observed (Fig EV2J–L); however, an observation that seems inconsistent with the proposed role of MAD1 as a CENP-E receptor (Akera et al, 2015).

R^{EE}ZZ bypasses the requirements for CENP-E and MPS1 kinase activity

RZZS depends on CENP-E for its kinetochore localization when MPS1 is inhibited. We reasoned that this requirement for CENP-E to recruit RZZS in the absence of MPS1 kinase activity would be bypassed if MPS1 phosphorylation triggering of corona expansion could be mimicked. Phosphorylation of T13 and S15 on ROD by MPS1 is a prerequisite for corona expansion and RZZS polymerization (Rodriguez-Rodriguez et al, 2018; Raisch et al, 2022). In filamentation assays in vitro, mutation of these two residues to glutamic acid (E) allows RZZS polymerization in the absence of MPS1, while mutation to alanine (A) prevents polymerization even

in the presence of MPS1 kinase activity (Raisch et al, 2022). Thus, we performed experiments to assess if a mutant RZZ carrying T13E and S15E mutations on ROD (hereafter referred to as R^{EE}ZZ) bypasses a requirement for MPS1 activity for corona polymerization in cells. Contrary to electroporated wild type mCherry-RZZ, which was recruited to kinetochores but did not expand a corona in the presence of reversine, electroporated mCherry-R^{EE}ZZ expanded in a crescent shape even after inhibition of MPS1 (Fig 4A and B; expansion of the corona indicates that electroporated RZZ interacts with endogenous Spindly). Importantly, electroporated mCherry-R^{EE}ZZ succeeded in assembling the corona even in reversine treated cells additionally depleted of CENP-E and Zwilch by RNAi (Fig 4C–E). This observation provides an unequivocal demonstration that corona assembly harnesses a kinetochore receptor distinct from CENP-E. R^{EE}ZZ was removed in a timely manner upon biorientation (Fig EV4A–D), suggesting that the reversal of MPS1 phosphorylation of ROD may not be strictly required for corona disassembly.

MPS1 promotes the kinetochore recruitment of RZZS

Besides preventing corona expansion, MPS1 inhibition causes a reduction in the kinetochore levels of RZZS (Fig EV2A–D). Whether this reduction reflects a second role of MPS1 (in addition to corona expansion) in promoting kinetochore localization of RZZS is unknown. To investigate this, we tried to block corona expansion by means other than MPS1 inhibition. In humans and nematodes corona expansion requires a negatively charged cluster on Zwilch that contains two conserved residues, Glu422 and Asp426 (Fig 4B). Mutation of these residues to alanine prevents corona expansion (Gama et al, 2017; Pereira et al, 2018). Furthermore, RZ$^{E422A/D426A}$Z (hereafter referred to as RZ^{AA}Z) bound Spindly but was unable to form polymers in vitro (Raisch et al, 2022). In line with these previous observations, RZ^{AA}Z electroporated in cells depleted of endogenous Zwilch decorated kinetochores, albeit at slightly reduced levels, but was unable to promote corona expansion (Fig EV4E and F). We then applied the protocol described in Fig 4C to compare the localization of mCherry-RZZ^{WT},

Figure 4. MPS1 contributes to RZZS recruitment in addition to corona expansion.

A Representative images showing HeLa cells electroporated with the indicated ^{mCh}RZZ constructs. Before fixation, cells were synchronized in the G2 phase with 9 μM RO3306 for 15 h and then released into mitosis. Subsequently, cells were immediately treated with 3.3 μM Nocodazole, 10 μM MG132 and, where indicated, with 500 nM reversine, for an additional hour. CENP-C was used to visualize the kinetochores and DAPI to stain DNA. Three biological replicates were performed. Scale bar: 5 μm.

B A schematic of the ^{mCh}RZZ constructs utilized in panel D.

C A schematic of the cell synchronization and imaging experiment shown in panels D–G.

D Representative images showing the localization of Zwilch in prometaphase after depletion of CENP-E with 60 nM siRNA and Zwilch with 100 nM siRNA as shown schematically in panel C. Thirteen hours after CENP-E RNAi treatment HeLa cells were electroporated with mCherry or different ^{mCh}RZZ constructs as indicated. Following an 8 h recovery, cells were synchronized in the G2 phase with 9 μM RO3306 for 15 h and then released into mitosis. Subsequently, cells were immediately treated with 3.3 μM Nocodazole, 10 μM MG132 and, where indicated, with 500 nM reversine, for an additional hour. CENP-C was used to visualize kinetochores and DAPI to stain DNA. Three biological replicates were performed. Scale bar: 5 μm.

E–G Quantification of mCherry and Zwilch levels at kinetochores of the experiment shown in panel D. n refers to individually measured kinetochores.

H A schematic of the cell synchronization and imaging experiment shown in panels I–K.

I Representative images showing the localization of Zwilch in prometaphase after depletion of CENP-E with 60 nM siRNA and Spindly with 50 nM siRNA as shown schematically in panel H. Thirteen hours after CENP-E RNAi treatment HeLa cells were electroporated with electroporation buffer or ^{mCh}R^{EE}ZZ. Following an 8 h recovery, cells were synchronized in the G2 phase with 9 μM RO3306 for 15 h and then released into mitosis. Subsequently, cells were immediately treated with 3.3 μM Nocodazole, 10 μM MG132 and, where indicated, with 500 nM reversine, for an additional hour. CENP-C was used to visualize kinetochores and DAPI to stain DNA. Two biological replicates were performed. Scale bar: 5 μm.

J, K Quantification of mCherry and Zwilch levels at kinetochores of the experiment shown in panel I. n refers to individually measured kinetochores.

Data information: Statistical analysis (panels E, G, J, and K) was performed with a nonparametric t-test comparing two unpaired groups (Mann–Whitney test). Symbols indicate: $^{n.s.}P > 0.05$, $*P \le 0.05$, $**P \le 0.01$, $***P \le 0.001$, $****P \le 0.0001$. Red bars represent the median and interquartile range.
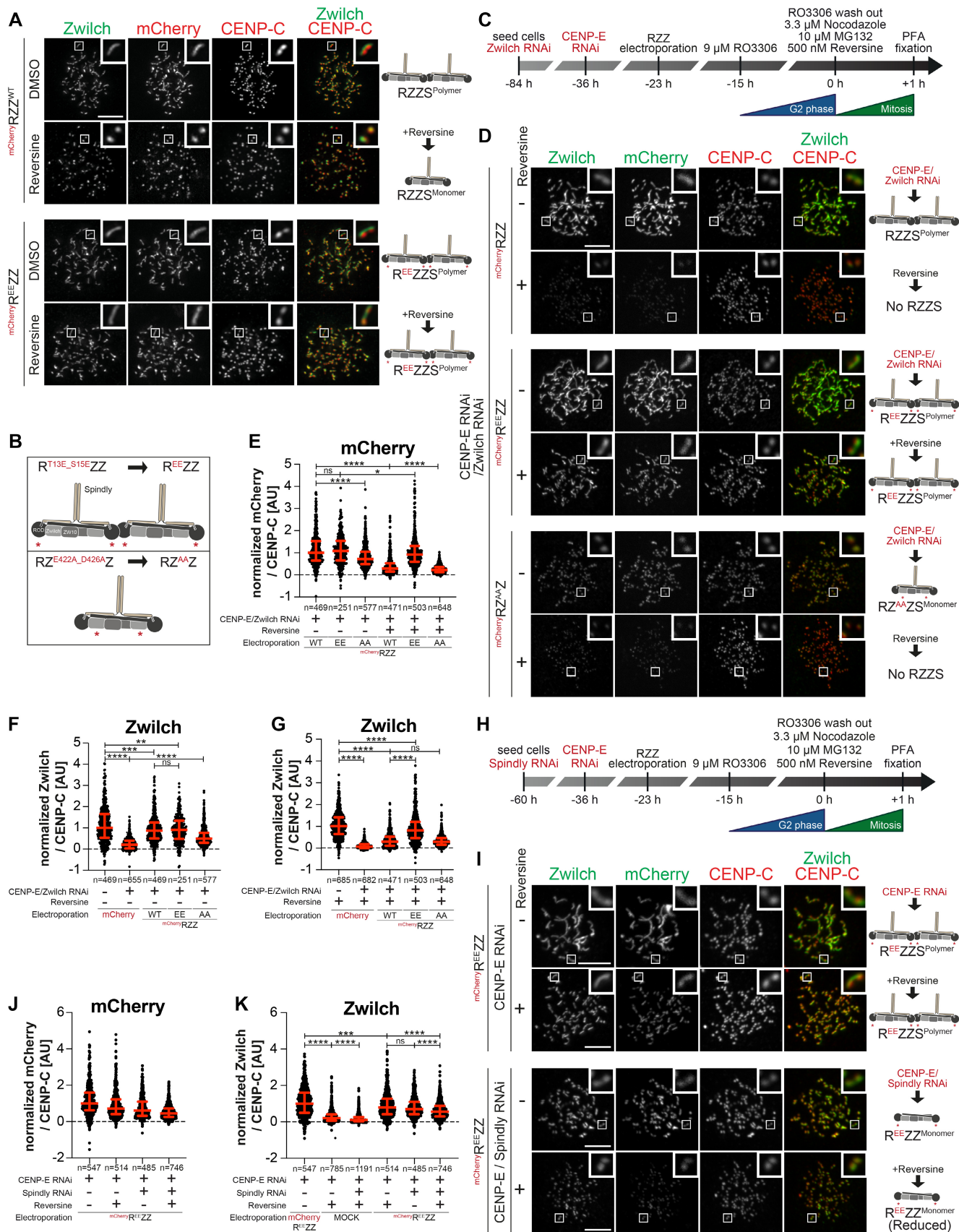
Figure 4.

mCherry-R^{EE}ZZ, and mCherry-RZ^{AA}Z in the presence or absence of reversine in cells depleted of endogenous CENP-E and RZZ. Contrary to mCherry-R^{EE}ZZ, MPS1 inhibition entirely prevented RZ^{AA}Z from being recruited to the kinetochore (Fig 4D–G). Thus, RZ^{AA}Z decouples the effects of inhibiting MPS1 from those resulting from inhibition of corona expansion. Its behavior suggests that MPS1, in addition to corona expansion, additionally promotes the kinetochore recruitment of RZZ. Robust kinetochore recruitment of the phosphomimetic mCherry-R^{EE}ZZ mutant despite MPS1 inhibition also suggests that this additional function of MPS1 is dispensable if corona expansion can proceed.

To confirm this conclusion, we turned to two additional conditions known to prevent corona expansion, the mutation of T13 and S15 to non-phosphorylatable alanine residues and the depletion of Spindly (Rodriguez-Rodriguez *et al*, 2018; Raisch *et al*, 2022). Electroporated R$^{T13A/S15A}$ZZ (abbreviated as R^{AA}ZZ and not to be confused with RZ^{AA}Z) decorated kinetochores but did not expand the corona in cells depleted of CENP-E and endogenous Zwilch. Confirming our model, inhibition of MPS1 caused an essentially complete depletion of R^{AA}ZZ from kinetochores (Fig EV4G–I). Depletion of Spindly in cells also depleted of CENP-E was also compatible with robust RZZ recruitment, but corona expansion was inhibited. Further inhibition of MPS1 led to a complete depletion of endogenous Zwilch from the kinetochore (Appendix Fig S3A and B). Even in cells harboring electroporated R^{EE}ZZ, depletion of Spindly and CENP-E prevented corona expansion. Further addition of reversine caused a strong reduction in the kinetochore levels of R^{EE}ZZ (Fig 4H–K). Thus, when corona polymerization is prevented, even R^{EE}ZZ becomes sensitive to the MPS1 inhibition for kinetochore localization. We conclude that MPS1 promotes the recruitment of RZZ to a currently unknown kinetochore receptor.

CENP-E contributes to the kinetochore recruitment of the DD complex

While CENP-E becomes dispensable for robust corona expansion after MPS1-mediated phosphorylation of RZZS, it may continue to interact with, and influence the function of, the RZZS even after corona expansion. As discussed in the Introduction, a primary function of RZZS is to bind and activate DD. DD adaptors have been previously proposed to be a fulcrum for co-regulation of DD and kinesin activity (see the Discussion section). Thus, we decided to investigate if CENP-E influenced DD activity at the kinetochore. Supporting this hypothesis, RNAi-mediated depletion of CENP-E caused a very substantial reduction of p150^{glued} (a subunit of dynactin, hereafter simply referred to as p150) at kinetochores in prometaphase arrested cells (Fig 5A–D). The normal levels of p150 were restored after electroporation of recombinant CENP-E^{2070C} but not of the RZZS^{Mut} mutant. Further quantifications indicated that this effect was not a mere consequence of the lower kinetochore levels of RZZS^{Mut} relative to the wild type CENP-E^{2070C} that we demonstrated in Fig 2D and E (Appendix Fig S4A and B). Thus, our results suggest that binding of CENP-E to the RZZS complex is required for full accumulation of DD. Thus, in addition to the RZZS complex, CENP-E also contributes substantially to DD recruitment, and possibly activation, at the kinetochore. Of note, these changes in the levels of DD did not affect the levels of Spindly, which remained largely unaltered (quantified in Fig 5D), implying that CENP-E does not contribute to DD recruitment by controlling the levels of Spindly.

Spindly contains various sequence elements implicated in its function and regulation as a DD adaptor (Fig 5E). In our previous work, we reported that Spindly may exist in an autoinhibited conformation (see model in Fig EV5A) and proposed that an unknown

---

Figure 5. CENP-E is important for DD kinetochore recruitment.

A   A schematic representation of the cell synchronization protocols for the experiment in panels B–D.

B   Representative images showing the localization of dynactin monitored through the p150^{glued} subunit after depletion of CENP-E with 60 nM siRNA. Thirteen hours after RNAi treatment HeLa cells were electroporated with electroporation buffer or recombinant ^{EGFP}CENP-E^{2070C} constructs as indicated. Following an 8 h recovery, cells were synchronized in the G2 phase with 9 µM RO3306 for 15 h and then released into mitosis. Subsequently, cells were immediately treated with 3.3 µM Nocodazole for an additional hour. CENP-C was used to visualize kinetochores and DAPI to stain DNA. Three biological replicates were performed. Scale bar: 5 µm.

C, D   Quantification of dynactin-p150^{glued} and Spindly levels at kinetochores of the experiment shown in panel B. *n* refers to individually measured kinetochores.

E   A schematic representation of the organization of Spindly and relevant coiled-coil prediction.

F   A schematic representation of the cell synchronization protocols for the experiment in panels G–I.

G   Representative images showing the localization of dynactin monitored through the p150^{glued} subunit after depletion of Spindly with 50 nM siRNA. Thirty-seven hours after RNAi treatment, HeLa cells were electroporated with electroporation buffer or recombinant ^{mCh}Spindly constructs as indicated. Following an 8 h recovery, cells were synchronized in the G2 phase with 9 µM RO3306 for 15 h and then released into mitosis. Subsequently, cells were immediately treated with 3.3 µM Nocodazole for an additional hour. CENP-C was used to visualize kinetochores and DAPI to stain DNA. Three biological replicates were performed. Scale bar: 5 µm.

H, I   Quantification of Spindly and dynactin-p150^{glued} levels at kinetochores of the experiment shown in panel G. *n* refers to individually measured kinetochores.

J   A schematic representation of the cell synchronization protocols for the experiment in panels K–M.

K   Representative images showing the localization of dynactin monitored through the p150^{glued} subunit after depletion of CENP-E with 60 nM siRNA and Spindly with 50 nM siRNA. Thirteen hours after CENP-E RNAi treatment HeLa cells were electroporated with electroporation buffer or recombinant ^{mCh}Spindly constructs as indicated. Following an 8 h recovery, cells were synchronized in the G2 phase with 9 µM RO3306 for 15 h and then released into mitosis. Subsequently, cells were immediately treated with 3.3 µM Nocodazole for an additional hour. CENP-C was used to visualize kinetochores and DAPI to stain DNA. Three biological replicates were performed. Scale bar: 5 µm.

L, M   Quantification of mCherry and dynactin-p150^{glued} levels at kinetochores of the experiment shown in panel K. *n* refers to individually measured kinetochores.

Data information: Statistical analysis (C and D, H and I, and L and M) was performed with a nonparametric *t*-test comparing two unpaired groups (Mann–Whitney test). Symbols indicate: $^{n.s.}P > 0.05$, $*P \leq 0.05$, $**P \leq 0.01$, $***P \leq 0.001$, $****P \leq 0.0001$. Red bars represent the median and interquartile range.
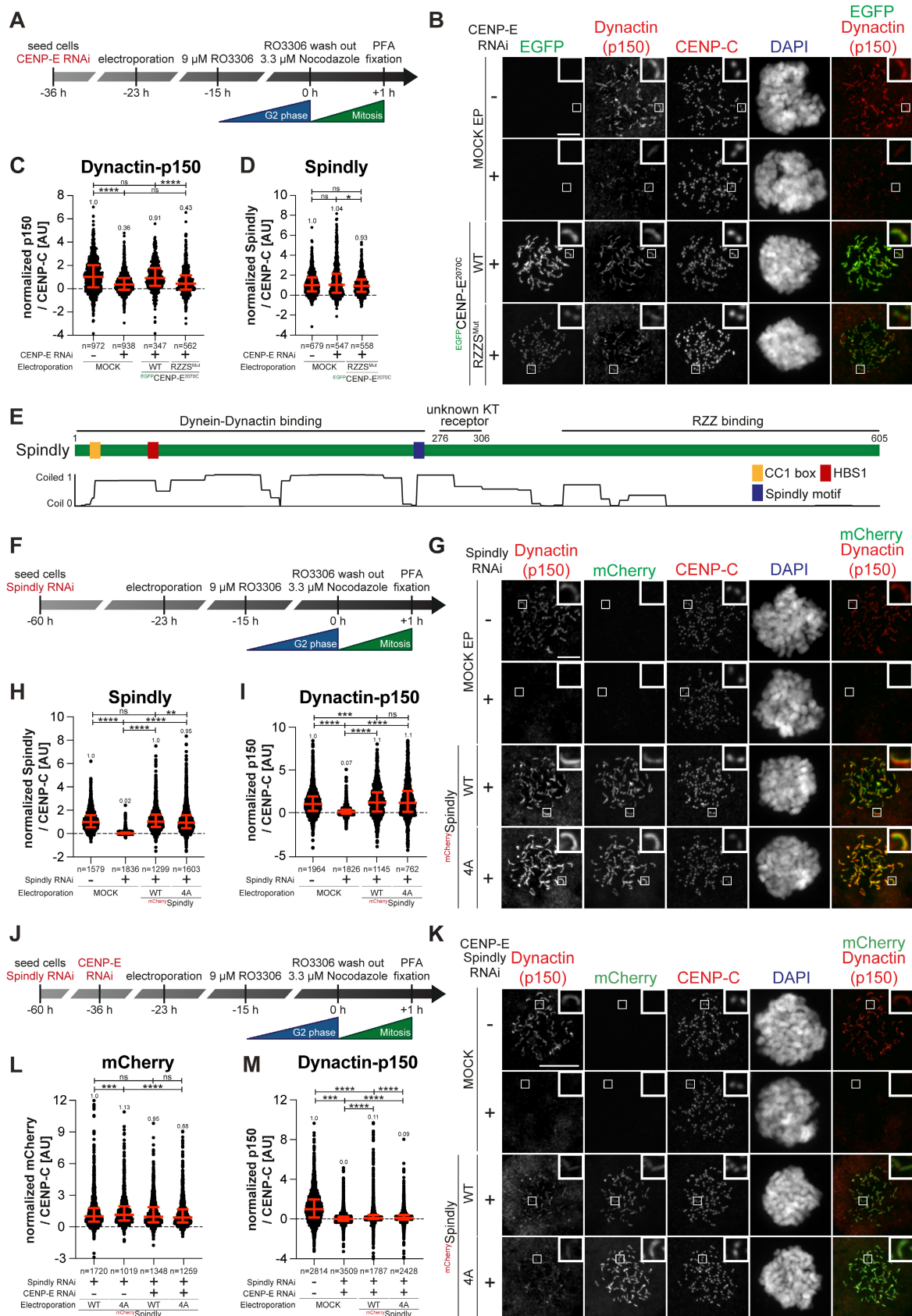
Figure 5.

kinetochore trigger promotes a conformational change required for efficient binding of Spindly to DD at the kinetochore (d'Amico *et al*, 2022). The Spindly motif, identified in Spindly and other DD adaptors (Fig 5E), promotes an interaction with the pointed-end (PE) subcomplex of dynactin (Gassmann *et al*, 2010; Gama *et al*, 2017). In agreement with our model that Spindly is natively autoinhibited, mCherry-Spindly did not bind PE in SEC experiments (Fig EV5B). In our previous work, we also described mutants of Spindly that overcome autoinhibition and bind PE (d'Amico *et al*, 2022). These mutants, however, were not recruited effectively to kinetochores, presumably because the mutated residues (in the 276–306 region of Spindly) also affected the interaction of Spindly with an unknown kinetochore receptor (Barisic *et al*, 2010; d'Amico *et al*, 2022). We therefore generated additional mutants to identify a separation-of-function mutant that would relieve Spindly autoinhibition without affecting kinetochore recruitment. Contrary to Spindly^{WT}, a Spindly^{4A} mutant (described in Fig EV5A) interacted with the PE complex in a SEC experiment (Fig EV5B and C), suggesting autoinhibition has been at least partially relieved. Spindly^{4A}, but not Spindly^{WT}, also interacted with CENP-E in SEC experiments, albeit weakly (Fig EV5D and E). Importantly, in cells depleted of endogenous Spindly, electroporated mCherry-Spindly^{4A} localized to the corona indistinguishably from its wild type counterpart and recruited DD (Fig 5F–I).

These observations suggest that we might have obtained an open mutant of Spindly that can also be efficiently recruited to the kinetochore, thus outperforming our previously described mutants (d'Amico *et al*, 2022). We used this mutant to test the idea that CENP-E triggers a conformational change that relieves Spindly autoinhibition to promote binding to and the kinetochore recruitment of DD. In this model, Spindly^{4A}, if effectively open, might overcome the deleterious effects of CENP-E depletion on DD recruitment. Contrary to our hypothesis, however, Spindly^{4A}, even if normally recruited to kinetochores in the absence of CENP-E, did not rescue the defect on DD recruitment caused by CENP-E depletion (Fig 5J–M). Thus, Spindly^{4A} is insufficient to rescue the effects on dynactin recruitment caused by depletion of CENP-E. Another open Spindly construct, Spindly$^{33–605}$ (lacking the first 32 residues containing the Spindly CC1 box, also required for autoinhibition) (d'Amico *et al*, 2022) also localized normally to kinetochores and rescued dynactin levels upon depletion of endogenous Spindly. Yet, like Spindly^{4A}, this mutant was unable to recruit dynactin in the absence of CENP-E (quantified in Fig EV5F and G). Collectively, these results suggest either that Spindly^{4A} and Spindly$^{33–605}$ are not fully "open" or that they are, but CENP-E is required for DD recruitment in addition to any putative function on Spindly opening.

As depletion of CENP-E led to a very significant but incomplete depletion of dynactin, we asked if the residual dynactin was recruited through CENP-F, which has been shown to participate in the recruitment of DD to the kinetochore and corona compaction (Vergnolle & Taylor, 2007; Gassmann, 2023; Mitevska *et al*, 2023). While CENP-F depletion had insignificant effects on the kinetochore levels of dynactin, its combination with CENP-E depletion led to an almost complete depletion of kinetochore dynactin (Fig EV5H–K), with the residual dynactin signal probably reflecting recruitment by Spindly. Thus, recruitment of DD to the kinetochore may reflect concomitant interactions with RZZS, CENP-E, and CENP-F.

Discussion

We discovered an interaction of CENP-E and RZZS that controls the recruitment and activation of DD at the kinetochore. By harnessing various separation of function mutants, we brought to light several new points of contact of the corona with the kinetochore. After our new characterization, the corona assembly plan of Fig 1B is in need of significant revision (Fig 6A). Our main results can be summarized in the following points. First, BUBR1 and RZZS play a highly prominent role in CENP-E recruitment. The interaction of CENP-E with BUBR1 had been described earlier (Mao *et al*, 2003, 2005; Ciossani *et al*, 2018; Legal *et al*, 2020). This interaction of CENP-E is clearly orthogonal to that with the RZZS complex, as it engages a different region of CENP-E and is sufficient for recruitment of CENP-E to kinetochores when the RZZS-binding site is mutated. The interaction with BUBR1 is dispensable for the kinetochore recruitment of CENP-E in prometaphase, when CENP-E is clearly identified in the corona, but becomes essential for the kinetochore recruitment of CENP-E after corona shedding, an event that coincides with biorientation (Fig 6B). Whether CENP-E is simultaneously bound to BUBR1 and the RZZS complex remains to be established. The observation that BUBR1 does not integrate into the corona may suggest the existence of two distinct pools of CENP-E. However, CENP-E is highly elongated (Kim *et al*, 2008), and its long axis may transverse the depth of the kinetochore, interacting with the RZZS complex within the corona but extending further inside the kinetochore to interact with BUBR1.

Constructs carrying both BUBR1^{Mut} and RZZS^{Mut} were unable to localize to kinetochores. Conversely, depletion of BUBR1 and RZZS largely reduced kinetochore CENP-E, but did not completely eliminate it. The residual levels of CENP-E may reflect incomplete depletion of RZZ and BUBR1 or the existence of a third, currently unknown receptor. In line with at least two earlier studies (Sharp-Baker & Chen, 2001; Martin-Lluesma *et al*, 2002), we did not find evidence for an involvement of MAD1 in the recruitment of CENP-E (Akera *et al*, 2015). Specifically, we found that a condition that largely reduced kinetochore MAD1 did not grossly affect CENP-E recruitment.

Second, RZZS and CENP-E are co-dependent for their own kinetochore recruitment (Fig 6C). In previous work, we and others had shown that the depletion of CENP-E did not prevent corona assembly (Martin-Lluesma *et al*, 2002; Ciossani *et al*, 2018). Here, we confirmed this conclusion with a cell line that allows the acute depletion of CENP-E (Owa & Dynlacht, 2021). However, depletion of CENP-E caused complete depletion of RZZS from kinetochores when combined with inhibition of MPS1 kinase. MPS1 has been previously shown to promote corona expansion by phosphorylating ROD (Rodriguez-Rodriguez *et al*, 2018; Raisch *et al*, 2022). These results indicate to us that MPS1, through corona expansion, through the facilitation of a direct interaction, or both, promotes binding of RZZS to one or more kinetochore receptors, in addition to CENP-E. We refer to this receptor or receptors as "core kinetochore receptor" of RZZS.

Third, MPS1, in addition to an established role in corona expansion through ROD phosphorylation (Rodriguez-Rodriguez *et al*, 2018; Raisch *et al*, 2022), indeed has a distinct function in promoting binding of RZZS to its core kinetochore receptor (Fig 6D). This additional function of MPS1 became evident when
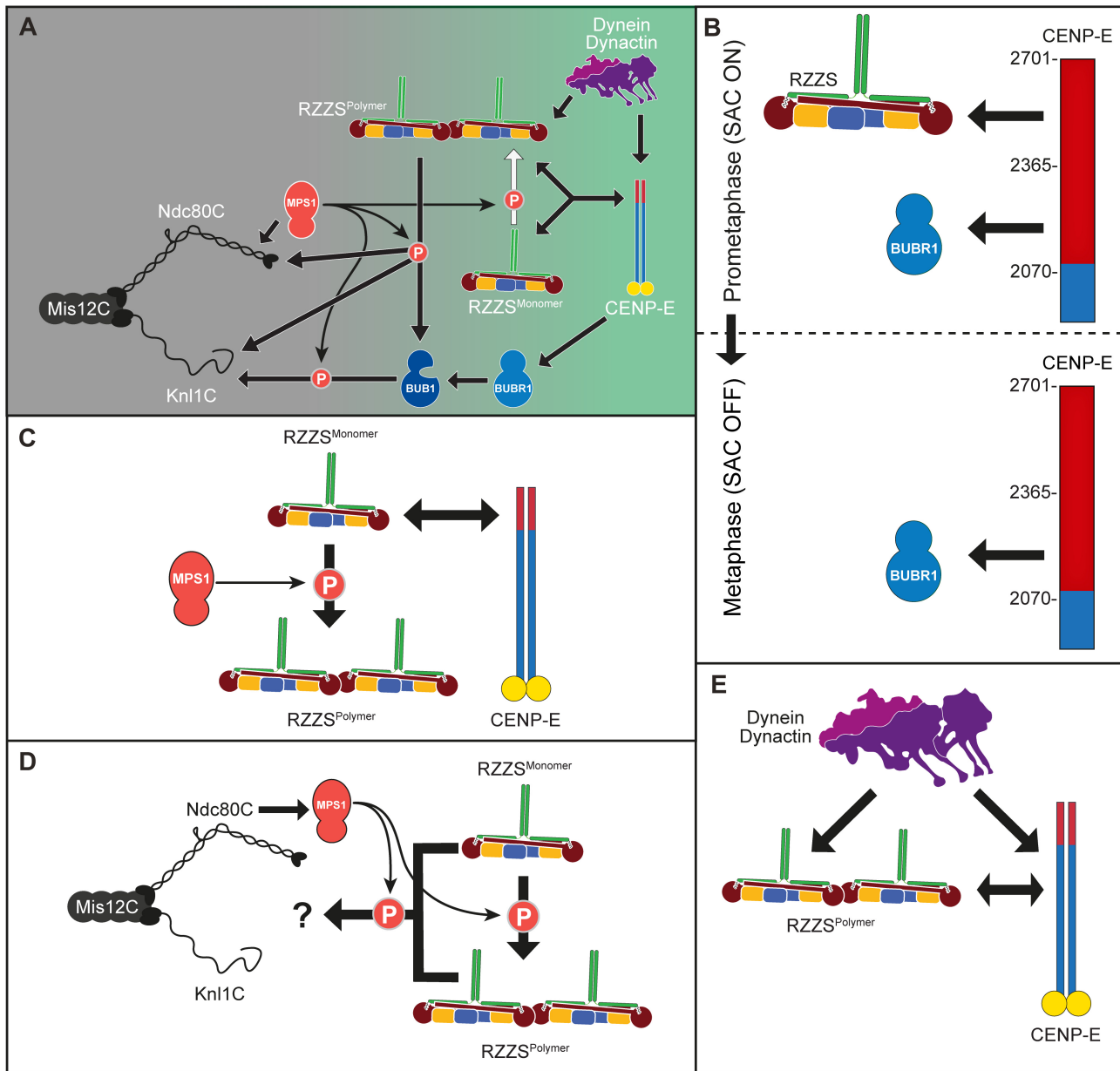
Figure 6. Summary of the main results.

A   Revised drawing depicting the hierarchical organization of outer kinetochore and kinetochore corona components after our study. Compare with Fig 1B. Thick arrows indicate recruitment of a protein to the protein indicated by the arrowhead. Thin arrows indicate phosphorylation. The white arrow indicates polymerization.

B–E Depiction of individual interactions in the order in which they are presented in the "Discussion" section.

CENP-E depletion was combined with inhibition of corona expansion by means other than inhibiting MPS1, including expressing mutants of ROD or Zwilch, or depleting Spindly. Like MPS1 inhibition, these conditions did not prevent RZZS (or RZZ) kinetochore recruitment. Further inhibition of MPS1, however, abrogated RZZS or RZZ localization. Thus, lack of corona expansion with these alternative perturbations does not fully recapitulate the effects of inhibiting MPS1, indicating that MPS1, in addition to corona expansion, promotes binding of RZZS to its core kinetochore receptor. Importantly, the R^{EE}ZZ mutant was insensitive to MPS1 inhibition and CENP-E depletion, and expanded a robust corona. Because R^{EE}ZZ interacts with kinetochores when corona expansion and MPS1 are both inhibited (and in the absence of CENP-E), we suspect that phosphorylation of Thr13 and Ser15, in addition to causing corona expansion, also mediates an interaction with the core kinetochore receptor. Further investigation of this issue will require the identification and a detailed investigation of the core kinetochore receptor of RZZS.

Fourth, the co-dependent localization of RZZS and CENP-E is especially meaningful for robust DD recruitment to the kinetochore (Fig 6E). Previously, we have garnered evidence that Spindly, as a DD adaptor at the kinetochore, requires a kinetochore stimulus to "open up" from an auto-inhibited conformation (d'Amico *et al*, 2022). However, Spindly mutants that we suspect to be in an open conformation based on their ability to interact with the pointed-end complex of dynactin do not rescue the reduction of DD caused by CENP-E depletion. Thus, while we cannot conclude or exclude that CENP-E is the factor that "opens" Spindly at the kinetochore, we can argue that it is additionally required downstream of Spindly opening, possibly through a direct interaction stabilizing DD at the kinetochore. In the future, we will try to use biochemical reconstitution to gain further support for this model and identify the detailed determinants of this regulation. Our results also imply that depletion of CENP-E, by causing a significant co-depletion of DD, may have distinct and more pervasive effects on chromosome alignment than the sole inhibition of CENP-E with small molecule inhibitors (Wood *et al*, 2010; Ohashi *et al*, 2015).

While until now the corona has been primarily viewed as a platform for the coordination of dynein motility and spindle assembly checkpoint activity (Kops & Gassmann, 2020; Gassmann, 2023), our results indicate that it should be instead regarded as an extended adaptor for opposite-polarity motors. The corona combines DD and CENP-E in a single integrated complex capable of bidirectional transport of chromosomes as cargo. Integration of minus- and plus-end-directed microtubule motor activity may be a common theme of transport for other categories of cargo, including lysosomes or secretory vesicles among others (Kendrick *et al*, 2019; preprint: Canty *et al*, 2021; Fenton *et al*, 2021; Celestino *et al*, 2022). TRAK1/2 adaptors, for instance, promote the incorporation of kinesin-1 (Kif5) and DD in a single complex (preprint: Canty *et al*, 2021; Fenton *et al*, 2021). Kinesin-1 binds a region of TRAK that contains the CC1 box, a DD binding region that we have also implicated in the intramolecular regulation of Spindly (Randall *et al*, 2013; d'Amico *et al*, 2022). CENP-E may contribute to the activation of Spindly in a similar manner, in addition to a more direct role in DD binding. Collectively, our studies and the recent observations on the interactions of DD adaptors with kinesins seem to suggest that in addition to bringing dynein and dynactin into the same complex (Carter *et al*, 2016; Reck-Peterson *et al*, 2018; Olenick & Holzbaur, 2019), a more general function of adaptors and associated proteins is to bring DD and cognate kinesins into the same complex. A previous study had reported the association of a minus-end directed motor with CENP-E in mitotic HeLa extract, but excluded that the activity might be due to DD (Thrower *et al*, 1995). Our findings suggest that this conclusion might have been premature.

End-on attachment may be an active process where the DD module directly controls the engagement of the Ndc80C (Cheerambathur *et al*, 2013). What triggers corona shedding upon end-on attachment, however, remains poorly understood. Importantly, shedding will also deplete kinetochores of the MAD1:MAD2 core complex crucially required for checkpoint signaling, thus beginning checkpoint silencing (De Antoni *et al*, 2005; Fava *et al*, 2011; Maldonado & Kapoor, 2011; Luo *et al*, 2018). Autoinhibition of kinesin-1 has been shown to facilitate the initiation of dynein cargo transport (Qiu *et al*, 2023). Similarly, the transition to pole-directed transport of kinetochore proteins during shedding may reflect initiation of dynein cargo transport when the activity of CENP-E becomes suppressed. The relief from autoinhibition that prefigures the activation of CENP-E motor activity may require phosphorylation by mitotic kinases, including MPS1 and CDK1 (Nousiainen *et al*, 2006; Espeut *et al*, 2008). Aurora A and Aurora B, kinases residing primarily at spindle poles and centromeres, respectively, may further contribute to CENP-E activation by phosphorylating Thr422. This residue is encompassed within a binding motif for protein phosphatase 1 (PP1), whose phosphorylation counteracts PP1 recruitment (Egloff *et al*, 1997; Kim *et al*, 2010; Liu *et al*, 2010). Upon dephosphorylation, docking of PP1 to T422 may promote further CENP-E dephosphorylation and its subsequent autoinhibition (Kim *et al*, 2010). This, in turn, may initiate shedding. This model is attractive because Aurora B kinase has an established role in biorientation and is believed to be regulated by forces exerted by microtubules as they bind the kinetochore (Krenn & Musacchio, 2015; Lampson & Grishchuk, 2017). We note that the corona appeared to disassemble normally in the presence of the phosphomimetic R^{EE}ZZ mutant, suggesting that preventing dephosphorylation of the MPS1 sites may not be sufficient for retaining the corona. Changes in MPS1 or Aurora B activity upon biorientation, however, are likely to be relevant for shedding. Dephosphorylation of MPS1 sites may cause a reduction in the binding affinity of RZZS for its core kinetochore receptor, which we show to depend on MPS1 activity. Dephosphorylation of T422 of CENP-E and other Aurora B sites, by causing conformational changes in CENP-E, may also affect its ability to hold onto the corona (Eibes *et al*, 2023).

The identification of binding determinants is a prerequisite for the dissection of their dynamic regulation and for the generation of adequate separation-of-function mutants. In this study, we have identified several new interactions that are essential for the establishment of the kinetochore corona. Understanding the regulation of these interactions will contribute to dissecting the basis for the coordination of chromosome biorientation and checkpoint silencing. Our work sets the stage for future investigations of the dauntingly complex processes that enforce correct chromosome segregation.

Materials and Methods

Mutagenesis and cloning

The codon-optimized cDNA of CENP-E (Q02224) was synthesized at GeneWiz and subcloned in pLIB-EGFP and pET-EGFP, modified versions of, respectively, the pLIB (Weissmann *et al*, 2016) and pET-28 vector for expression of proteins with N-terminal PreScission-cleavable His$_6$-EGFP-tag. Mutations were introduced by site-directed mutagenesis and Gibson assembly (Gibson *et al*, 2009) and verified by Sanger sequencing (Microsynth Seqlab). The Spindly constructs were generated as previously described (d'Amico *et al*, 2022) and subcloned in pLIB with an N-terminal His$_6$-mCherry-tag.

Expression and purification of RZZ and Spindly constructs

The RZZ complex was expressed and purified using the biGBac system (Weissmann *et al*, 2016), with a mCherry-tag on the N-terminus of the ROD subunit, as previously described (Sacristan *et al*, 2018; Raisch *et al*, 2022). All mCherry–Spindly constructs, except for

Spindly[33–605], were expressed using the biGBac system. Spindly[33–605] was expressed in *Escherichia coli* (*E. coli*) and purified as described (d'Amico *et al*, 2022). The Baculovirus was generated in Sf9 cells to infect Tnao38 cells, which were grown for 72 h at 27°C before harvesting. The pellet was washed with PBS, snap-frozen and stored at −80°C. Purification of the Spindly constructs was performed as previously described (d'Amico *et al*, 2022) The pellet was resuspended in lysis buffer (50 mM HEPES pH 8.0, 250 mM NaCl, 30 mM imidazole, 2 mM Tris(2-carboxyethyl)phosphine (TCEP) supplemented with protease inhibitor, 1 mM PMSF, DnaseI and lysed by sonication). The lysate was clarified by centrifugation for 45 min at 88,000 *g*, sterile filtered and loaded onto a HisTrap HP column (Cytiva). Subsequently, the column was washed with at least 20 column volumes lysis buffer. Elution was performed with lysis buffer supplemented with 300 mM imidazole. The eluate was diluted 1:5 in no salt buffer (50 mM HEPES pH 8.0, 2 mM TCEP), and applied to a 6 ml Resource Q-anion exchange column (Cytiva). The protein was eluted with a 50–500 mM NaCl gradient, and fractions were analyzed by SDS–PAGE. Fractions containing the protein of interest were pooled and concentrated. Finally, the protein was loaded onto a Superdex 200 16/60 pre-equilibrated in SEC buffer (50 mM HEPES pH 8.0, 250 mM NaCl, 2 mM TCEP). Peak fractions containing the protein of interest were analyzed by SDS–PAGE, concentrated, snap-frozen, and stored at −80°C until further usage.

Expression and purification of the EGFP-CENP-E constructs

Expression of CENP-E[2070C] wild-type and mutants and CENP-E[2070–2365] was carried out in insect cells using the biGBac system. The Baculoviruses were generated in Sf9 cells to infect Tnao38 cells for 72 h at 27°C before harvesting. The pellet was washed with PBS, snap-frozen and stored at −80°C. For purification, CENP-E was resuspended in lysis buffer (50 mM HEPES pH 8.0, 250 mM NaCl, 5% (w/v) glycerol, and 1 mM TCEP) supplemented with protease inhibitor, 1 mM PMSF, DnaseI and lysed by sonication. The lysate was clarified by centrifugation for 45 min at 88,000 *g*, sterile filtered and loaded onto a HisTrap HP column (Cytiva). Elution was performed with lysis buffer supplemented with 300 mM imidazole. Subsequently, the CENP-E[2070C] mutants were diluted 1:5 in low salt buffer (50 mM HEPES pH 8.0, 50 mM NaCl, 5% (w/v) glycerol, 1 mM TCEP), and applied to a 6 ml Resource Q anion exchange column (Cytiva). The protein was eluted with a 50–500 mM NaCl gradient, and peak fractions were analyzed by SDS–PAGE. Fractions containing the protein of interest were pooled and concentrated. The concentrated sample was loaded onto a Superdex 200 16/60 pre-equilibrated in SEC buffer (50 mM HEPES pH 8.0, 250 mM NaCl, 5% (w/v) glycerol, 1 mM TCEP). Finally, peak fractions containing the protein of interest were analyzed by SDS–PAGE, concentrated, snap-frozen and stored at −80°C until further usage. CENP-E[2070–2365] and CENP-E[2070C] wild-type was loaded on a Superdex 200 16/60 directly after affinity purification. Peak fractions containing the protein of interest were analyzed by SDS–PAGE, concentrated, snap-frozen, and stored at −80°C until further usage.

EGFP-CENP-E[2366C] (WT and mutants) were expressed in *E. coli* BL21 (DE3) RP plus cells grown in Terrific-Broth (TB) at 37°C to $OD_{600} = 0.6$ and then induced for 16 h at 17°C with 0.25 mM isopropyl-beta-D-thiogalactopyranoside (IPTG). Cells were collected

by centrifugation, washed in PBS, and then frozen at −80°C. Cell pellets were resuspended in lysis buffer (50 mM sodium phosphate (Na_3PO_4) pH 7.0, 5% (w/v) glycerol, 2 mM β-mercaptoethanol (BME) and 500 mM NaCl) supplemented with protease inhibitor, lysed by sonication, and cleared by centrifugation at 70,000 *g* at 4°C. The supernatant was filtered and loaded on a 5 ml HisTrap FF column (GE Healthcare) equilibrated in lysis buffer. After washing with lysis buffer and 75 mM imidazole, the protein were eluted with 500 mM imidazole. Proteins were concentrated and gel-filtered on a Superose 6 10/30 (GE Healthcare) equilibrated in SEC buffer (50 mM HEPES pH 7.0, 200 mM NaCl, 5% (w/v) glycerol, 1 mM TCEP).

Expression and purification of the kinase domain of BUBR1 (BUBR1[KD]) construct was carried out as previously reported (Breit *et al*, 2015).

Analytical SEC

Binding assays of Spindly with CENP-E[2070C] and PE complex were performed under isocratic conditions on a Superdex 200 15/50 pre-equilibrated in SEC buffer (50 mM HEPES pH 8.0, 150 mM NaCl, 2 mM TCEP) at 4°C on an ÄKTAmicro system. Elution of proteins was monitored at 280 nm. 50 µl fractions were collected and analyzed by SDS–PAGE. To assess complex formation proteins were mixed at the indicated concentrations in 60 µl SEC buffer and incubated for at least 1 h on ice before the SEC assay was performed.

Binding assays of CENP-E and BUBR1 were carried out by mixing 16 µM CENP-E proteins with 8 µM BUBR1[KD] in a final volume of 30 µl. Binding assays were carried out under isocratic conditions on a Superose 6 5/150 or Superdex 200 5/150 (GE Healthcare) equilibrated with SEC buffer (50 mM HEPES pH 8.0, 100 mM NaCl, 5% (w/v) glycerol and 0.5 mM TCEP) at 4°C on an ÄKTAmicro system. Protein elution was monitored at 280 nm and 50 µl fractions were collected and analyzed by SDS–PAGE followed by Coomassie blue staining.

RZZS filament formation and imaging

RZZS filaments were formed essentially as described by d'Amico *et al* (2022). 4 µM mCherry-RZZ and 8 µM prefarnesylated Spindly was incubated overnight at room temperature in the presence of 1 µM GST-MPS1 in M-buffer (50 mM HEPES pH 7.5, 100 mM NaCl, 1 mM MgCl₂, 1 mM TCEP). Flow chambers were assembled by applying two strips of double-sided tape on a glass slide and then placing a standard coverslip on top. The sample was diluted 1:8 and EGFP-CENP-E constructs were added to a final concentration of 1 µM, promptly flowed into a flow chamber and imaged. Imaging was performed on a 3i Marianas system at 100× magnification. Sample images were acquired as five-stacks of *z*-sections at 0.27 µm, maximum-projected on the *z*-axis, and processed in Fiji.

RZZS rings formation and imaging

RZZS rings were formed by incubating 4 µM mCherry-RZZ with 8 µM prefarnesylated mCherry-Spindly in the presence of 1 µM GST-MPS1 in M-buffer (50 mM HEPES pH 7.5, 100 mM NaCl, 1 mM

MgCl$_2$, 1 mM TCEP). Flow chambers were assembled by placing two strips of double-sided tape on a glass slide and a pre-cleaned high-performance cleanroom cleaned 1.5H coverslip (Nexterion) on top. The flow chamber was maintained at room temperature for all subsequent steps. The chamber was first equilibrated in S-buffer (50 mM HEPES pH 8, 200 mM NaCl, 2 mM TCEP). Anti-mCherry GST-tagged nanobodies (Addgene #70696, Katoh *et al*, 2016) were expressed and purified according to published protocol (Katoh *et al*, 2016). The nanobody was diluted in 20 μl S-buffer to a final concentration of 1 μM, flowed through the chamber, and incubated for 5–10 min. The chamber was then washed with 20 μl S-buffer with 1% pluronic F-127 and incubated for 5 min. Following passivation, a wash was performed with 50 μl S-buffer with 0.1 mg/ml BSA (A-buffer) to saturate aspecific binding sites. The rings were diluted 1:100 in 20 μl A-buffer, flowed into the chamber, incubated for 5 min, and washed with A-buffer. EGFP-CENP-E and BUBR1 constructs were mixed and diluted to the specified concentrations in 20 μl A-buffer and flowed into the chamber, which was then promptly sealed and moved to the microscope for imaging. Imaging was performed on a VisiTIRF microscope in the 488 nm and 561 nm laser channels, at 100× magnification, in TIRF mode. Single images were taken with exposures of 100 or 200 ms. Images were visualized and cropped using Fiji.

Molecular modeling

CENP-E and Spindly predictions were generated using AlphaFold Multimer (preprint: Evans *et al*, 2021; Jumper *et al*, 2021) as previously described (d'Amico *et al*, 2022).

Mammalian plasmids

All mammalian plasmids were derived from pCDNA5/FRT/TO-EGFP-IRES, a previously modified version (Krenn *et al*, 2012) of the pCDNA5/FRT/TO vector (Invitrogen). To generate N-terminally-tagged EGFP-CENP-E constructs, the CENP-E sequence was obtained by PCR and subcloned in-frame with the EGFP-tag. All CENP-E constructs are RNAi-resistant and validated by Sanger sequencing (Microsynth Seqlab).

Cell lines

Parental Flp-In T-Rex DLD-1 osTIR1 cells were a kind gift from D. C. Cleveland (University of California, San Diego, USA). The hTERT-immortalized retinal pigment epithelial (hTERT-RPE-1) cell line in which both CENP-E alleles are C-terminally tagged with an AID and a 3×FLAG tag has been described (Owa & Dynlacht, 2021). The cell line expresses the plant E3 ubiquitin ligase osTIR1, which was stably integrated into the genome. Degradation of the endogenous CENP-E^{AID} is achieved through the addition of 500 μM IAA (Sigma-Aldrich) (Owa & Dynlacht, 2021).

Cell culture

HeLa, DLD-1 and RPE-1 cells were grown in Dulbecco's modified Eagle's medium (DMEM; PAN Biotech) supplemented with 10% tetracycline-free FBS (PAN Biotech), and L-Glutamine (PAN Biotech). Cells were grown at 37°C in the presence of 5% CO$_2$.

Generation of stable cell lines

Stable Flp-In T-Rex DLD-1 osTIR1 cell lines were generated using FRT/Flp recombination. CENP-E constructs were cloned into a pCDNA5/FRT/TO-EGFP-IRES plasmid and co-transfected with pOG44 (Invitrogen), encoding the Flp recombinase, into cells using X-tremeGENE (Roche) according to the manufacturer's instructions. Subsequently, cells were selected for 2 weeks in DMEM supplemented with hygromycin B (250 μg/ml; Carl Roth) and blasticidin (4 μg/ml; Thermo Fisher Scientific). Single-cell colonies were isolated, expanded and the expression of the transgenes was checked by immunofluorescence microscopy and immunoblotting analysis. The gene expression was induced by the addition of 0.01–0.3 μg/ml doxycycline (Sigma-Aldrich).

RNAi and drug treatment

Depletion of endogenous proteins was achieved through transfection of single small interfering RNA (siRNA) with RNAiMAX (Invitrogen) according to manufacturer's instructions. Following siRNAs treatments were performed in this study: 100 nM siBUBR1 (Dharmacon, 5′-CGGGCAUUUGAAUAUGAAA-3′) for 24 h, 60 nM siCENP-E (Dharmacon, 5′-AAGGCUACAAUGGUACUAUAU-3′) for 24 h, 50 nM siCENP-F (Dharmacon, 5′-CAAAGACCGGUGUUUAC-CAAG-3′; 5′-AAGAGAAGACCCCAAGUCAUC-3′) for 24 h, siSpindly (Sigma-Aldrich, 5′-GAAAGGGUCUCAAACUGAA-3′) for 48 h, 100 nM siZwilch (SMART pool from Dharmacon, L-019377-00-0005) for 72 h.

Unless indicated, Nocodazole (Sigma-Aldrich) was used at 3.3 μM, RO3306 (Calbiochem) at 9 μM, MG132 (Calbiochem) at 10 μM, and reversine (Cayman Chem.) at 500 nM.

Electroporation of recombinant protein into human cells

Recombinant mCherry–RZZ, mCherry–Spindly, or EGFP-CENP-E constructs were electroporated as previously described (Alex *et al*, 2019) using the Neon Transfection System Kit (Thermo Fisher Scientific). HeLa cells were trypsinized, washed with PBS, and resuspended in electroporation buffer R (Thermo Fisher Scientific). Recombinant protein was added to a final concentration of 7 μM in the electroporation slurry and electroporated by applying two consecutive 35-ms pulses with an amplitude of 1,000 V. Control cells were electroporated with mCherry or electroporation buffer, respectively. The electroporated sample was subsequently added to 15 ml of prewarmed PBS, centrifuged at 500 *g* for 5 min, and trypsinized for 5 min to remove noninternalized extracellular protein. After two additional PBS washing and centrifugation steps, the cell pellets were resuspended in prewarmed DMEM and seeded in a 6-well plate. Following an 8-h recovery, cells were treated with 9 μM RO3306 (Calbiochem) for 15 h. Subsequently, cells were released into mitosis in the presence of 3.3 μM Nocodazole for 1 h before fixation for immunofluorescence or harvesting for immunoblotting.

Immunofluorescence

Cells were grown on coverslips pre-coated with poly-L-lysine (Sigma-Aldrich). Before fixation, cells were pre-permeabilized with 0.5% Triton X-100 solution in PHEM (PIPES, HEPES, EGTA, MgSO$_4$)

buffer supplemented with 100 nM microcystin for 5 min before fixation with 4% PFA in PHEM for 20 min. For dynactin-p150^{glued} staining the cells were initially fixed with 4% PFA in PHEM for 5 min and then permeabilized for 10 min with PHEM supplemented with 0.5% Triton-X-100. After blocking with 5% boiled goat serum (BGS) in PHEM buffer for 1 h, cells were incubated for 2 h at room temperature with the following primary antibodies: BUBR1 (rabbit, Thermo Scientific #720297, 1:1,000), CENP-C (guinea pig, MBL, #PD030, 1:1,000), CENP-E (mouse, Abcam, ab5093, 1:200), CENP-F (rabbit, Novus NB500-101, 1:300), dynactin-p150^{glued} (mouse, BD Trans. Lab., #610473, 1:150), MAD1 labeled with DyLight488 (mouse, made in-house, Clone BB3-8, 1:200), Spindly (rabbit, Bethyl, #A301-354A, 1:1,000), Zwilch (rabbit, made in-house, #SI520, 1:900) diluted in 2.5% BGS-PHEM supplemented with 0.1% Triton-X-100. Subsequently, cells were incubated for 1 h at room temperature with the following secondary antibodies (all 1:200 in 2.5% BGS-PHEM supplemented with 0.1% Triton-X-100): Goat anti-mouse Alexa Fluor 488 (Invitrogen A A11001), goat anti-mouse Rhodamine Red (Jackson Immuno Research 115-295-003), donkey anti-rabbit Alexa Fluor 488 (Invitrogen A21206), donkey anti-rabbit Rhodamine Red (Jackson Immuno Research 711-295-152), goat anti-human Alexa Fluor 647 (Jackson Immuno Research 109-603-003), goat anti-guinea pig Alexa Fluor 647 (Invitrogen A-21450). All washing steps were performed with PHEM supplemented with 0.1% Triton-X-100 (PHEM-T) buffer. DNA was stained with 0.5 μg/ml DAPI (Serva) and Mowiol (Calbiochem) was used as mounting media.

Cell imaging

Cells were imaged at room temperature using a spinning disk confocal device on the 3i Marianas system equipped with an Axio Observer Z1 microscope (Zeiss), a CSU-X1 confocal scanner unit (Yokogawa Electric Corporation, Tokyo, Japan), 100×/1.4NA Oil Objectives (Zeiss), and Orca Flash 4.0 sCMOS Camera (Hamamatsu). Alternatively, cells were imaged using a 60× oil immersion objective lens on a DeltaVision deconvolution microscope (GE Healthcare, UK) equipped with an IX71 inverted microscope (Olympus, Japan), a PLAPON ×60/1.42 numerical aperture objective (Olympus) and a pco.edge sCMOS camera (PCO-TECH Inc., USA). Confocal images were acquired as *z*-sections at 0.27 μm (using Slidebook Software 6 from Intelligent Imaging Innovations). Images were converted into maximal intensity projections, converted into 16-bit TIFF files, and exported. Automatic quantification of single kinetochore or corona signals was performed using the software Fiji with background subtraction. The presented quantifications may demonstrate a large dispersion of values above the mean or median. Low values—including negative values—can be due background subtraction if the latter is high or the quantified signal is low. These negative values have no physical meaning, but we consider it more correct to retain them than to exclude them. The high values may be caused by overlapping ROIs, which are not infrequent in view of the very close spacing of kinetochores/coronas. Measurements were exported in Excel (Microsoft) and graphed with GraphPad Prism 9.0 (GraphPad Software). Statistical analysis was performed with a non-parametric *t*-test comparing two unpaired groups (Mann–Whitney test). Symbols indicate: $^{n.s.}P > 0.05$, $*P \leq 0.05$, $**P \leq 0.01$, $***P \leq 0.001$, $****P \leq 0.0001$. Figures were arranged using Adobe Illustrator 2022.

Immunoblotting

Mitotic cells were collected via shake-off and resuspended in lysis buffer (150 mM KCl, 75 mM HEPES pH 7.5, 1.5 mM EGTA, 1.5 mM MgCl$_2$, 10% (w/v) glycerol, and 0.075% NP-40 supplemented with protease inhibitor cocktail (Serva) and PhosSTOP phosphatase inhibitors (Roche)). After lysis, whole-cell lysates were centrifuged at 22,000 *g* for 30 min at 4°C. Subsequently, the supernatant was collected and resuspended in sample buffer for analysis by SDS–PAGE and Western blotting. The following primary antibodies were used: FLAG-tag (rabbit, Thermo Scientific, #PA1-984B, 1:1,000), GFP (rabbit, made in-house, 1:3,000), α-tubulin (mouse monoclonal, Sigma-Aldrich; 1:8,000). As secondary antibodies, anti-mouse or anti-rabbit (1:10,000; Amersham, NXA931 and NA934) conjugated to horseradish peroxidase were used. After incubation with ECL Western blotting reagent (GE Healthcare), images were acquired with the ChemiDoc MP System (Bio-Rad) using Image Lab 6.0.1 software.

Data availability

A selection of primary data for this paper has been deposited at Biostudies: S-BSST1211 (https://www.ebi.ac.uk/biostudies/studies/S-BSST1211).

Expanded View for this article is available online.

Author contributions

Andrea Musacchio: Conceptualization; supervision; funding acquisition; visualization; writing – original draft; project administration; writing – review and editing. **Verena Cmentowski:** Conceptualization; formal analysis; validation; investigation; visualization; writing – original draft; writing – review and editing. **Giuseppe Ciossani:** Conceptualization; investigation; writing – review and editing. **Ennio d'Amico:** Investigation; visualization; writing – review and editing. **Sabine Wohlgemuth:** Resources. **Brian Dynlacht:** Resources; writing – review and editing. **Mikito Owa:** Resources; writing – review and editing.

Disclosure and competing interests statement

The authors declare that they have no conflict of interest.

References

Akera T, Goto Y, Sato M, Yamamoto M, Watanabe Y (2015) Mad1 promotes chromosome congression by anchoring a kinesin motor to the kinetochore. *Nat Cell Biol* 17: 1124–1133

Alex A, Piano V, Polley S, Stuiver M, Voss S, Ciossani G, Overlack K, Voss B, Wohlgemuth S, Petrovic A *et al* (2019) Electroporated recombinant proteins as tools for in vivo functional complementation, imaging and chemical biology. *Elife* 8: e48287

Alfonso-Perez T, Hayward D, Holder J, Gruneberg U, Barr FA (2019) MAD1-dependent recruitment of CDK1-CCNB1 to kinetochores promotes spindle checkpoint signaling. *J Cell Biol* 218: 1108–1117

Allan LA, Camacho Reis M, Ciossani G, Huis In 't Veld PJ, Wohlgemuth S, Kops GJ, Musacchio A, Saurin AT (2020) Cyclin B1 scaffolds MAD1 at the kinetochore corona to activate the mitotic checkpoint. *EMBO J* 39: e103180

Ballister ER, Riegman M, Lampson MA (2014) Recruitment of Mad1 to metaphase kinetochores is sufficient to reactivate the mitotic checkpoint. *J Cell Biol* 204: 901–908

Barisic M, Sohm B, Mikolcevic P, Wandke C, Rauch V, Ringer T, Hess M, Bonn G, Geley S (2010) Spindly/CCDC99 is required for efficient chromosome congression and mitotic checkpoint regulation. *Mol Biol Cell* 21: 1968–1981

Basto R, Scaerou F, Mische S, Wojcik E, Lefebvre C, Gomes R, Hays T, Karess R (2004) In vivo dynamics of the rough deal checkpoint protein during Drosophila mitosis. *Curr Biol* 14: 56–61

Breit C, Bange T, Petrovic A, Weir JR, Muller F, Vogt D, Musacchio A (2015) Role of intrinsic and extrinsic factors in the regulation of the mitotic checkpoint kinase Bub1. *PLoS One* 10: e0144673

Caldas GV, Lynch TR, Anderson R, Afreen S, Varma D, DeLuca JG (2015) The RZZ complex requires the N-terminus of KNL1 to mediate optimal Mad1 kinetochore localization in human cells. *Open Biol* 5: 150160

Canty JT, Hensley A, Yildiz A (2021) TRAK adaptors coordinate the recruitment and activation of dynein and kinesin to control mitochondrial transport. *bioRxiv* https://doi.org/10.1101/2021.07.30.454553 [PREPRINT]

Carter AP, Diamant AG, Urnavicius L (2016) How dynein and dynactin transport cargos: a structural perspective. *Curr Opin Struct Biol* 37: 62–70

Celestino R, Gama JB, Castro-Rodrigues AF, Barbosa DJ, Rocha H, d'Amico EA, Musacchio A, Carvalho AX, Morais-Cabral JH, Gassmann R (2022) JIP3 interacts with dynein and kinesin-1 to regulate bidirectional organelle transport. *J Cell Biol* 221: e202110057

Chakraborty M, Tarasovetc EV, Zaytsev AV, Godzi M, Figueiredo AC, Ataullakhanov FI, Grishchuk EL (2019) Microtubule end conversion mediated by motors and diffusing proteins with no intrinsic microtubule end-binding activity. *Nat Commun* 10: 1673

Chan GK, Schaar BT, Yen TJ (1998) Characterization of the kinetochore binding domain of CENP-E reveals interactions with the kinetochore proteins CENP-F and hBUBR1. *J Cell Biol* 143: 49–63

Chan YW, Fava LL, Uldschmid A, Schmitz MH, Gerlich DW, Nigg EA, Santamaria A (2009) Mitotic control of kinetochore-associated dynein and spindle orientation by human Spindly. *J Cell Biol* 185: 859–874

Cheerambathur DK, Gassmann R, Cook B, Oegema K, Desai A (2013) Crosstalk between microtubule attachment complexes ensures accurate chromosome segregation. *Science* 342: 1239–1242

Cheeseman IM, Desai A (2008) Molecular architecture of the kinetochore-microtubule interface. *Nat Rev Mol Cell Biol* 9: 33–46

Cheeseman IM, Chappie JS, Wilson-Kubalek EM, Desai A (2006) The conserved KMN network constitutes the core microtubule-binding site of the kinetochore. *Cell* 127: 983–997

Ciossani G, Overlack K, Petrovic A, Huis In 't Veld PJ, Koerner C, Wohlgemuth S, Maffini S, Musacchio A (2018) The kinetochore proteins CENP-E and CENP-F directly and specifically interact with distinct BUB mitotic checkpoint Ser/Thr kinases. *J Biol Chem* 293: 10084–10101

Cooke CA, Schaar B, Yen TJ, Earnshaw WC (1997) Localization of CENP-E in the fibrous corona and outer plate of mammalian kinetochores from prometaphase through anaphase. *Chromosoma* 106: 446–455

Craske B, Legal T, Welburn JPI (2022) Reconstitution of an active human CENP-E motor. *Open Biol* 12: 210389

d'Amico EA, Ud Din Ahmad M, Cmentowski V, Girbig M, Muller F, Wohlgemuth S, Brockmeyer A, Maffini S, Janning P, Vetter IR *et al* (2022) Conformational transitions of the Spindly adaptor underlie its interaction with dynein and dynactin. *J Cell Biol* 221: e202206131

De Antoni A, Pearson CG, Cimini D, Canman JC, Sala V, Nezi L, Mapelli M, Sironi L, Faretta M, Salmon ED *et al* (2005) The Mad1/Mad2 complex as a template for Mad2 activation in the spindle assembly checkpoint. *Curr Biol* 15: 214–225

DeLuca JG, Gall WE, Ciferri C, Cimini D, Musacchio A, Salmon ED (2006) Kinetochore microtubule dynamics and attachment stability are regulated by Hec1. *Cell* 127: 969–982

Egloff MP, Johnson DF, Moorhead G, Cohen PT, Cohen P, Barford D (1997) Structural basis for the recognition of regulatory subunits by the catalytic subunit of protein phosphatase 1. *EMBO J* 16: 1876–1887

Eibes S, Rajendraprasad G, Guasch-Boldu C, Kubat M, Steblyanko Y, Barisic M (2023) CENP-E activation by Aurora A and B controls kinetochore fibrous corona disassembly. *Nat Commun* 14: 5317

Espeut J, Gaussen A, Bieling P, Morin V, Prieto S, Fesquet D, Surrey T, Abrieu A (2008) Phosphorylation relieves autoinhibition of the kinetochore motor Cenp-E. *Mol Cell* 29: 637–643

Evans R, O'Neill M, Pritzel A, Antropova N, Senior A, Green T, Žídek A, Bates R, Blackwell S, Yim J *et al* (2021) Protein complex prediction with AlphaFold-Multimer. *bioRxiv* https://doi.org/10.1101/2021.10.04.463034 [PREPRINT]

Fava LL, Kaulich M, Nigg EA, Santamaria A (2011) Probing the in vivo function of Mad1:C-Mad2 in the spindle assembly checkpoint. *EMBO J* 30: 3322–3336

Fenton AR, Jongens TA, Holzbaur ELF (2021) Mitochondrial adaptor TRAK2 activates and functionally links opposing kinesin and dynein motors. *Nat Commun* 12: 4578

Fischer ES (2022) Kinetochore-catalyzed MCC formation: a structural perspective. *IUBMB Life* 75: 289–310

Gama JB, Pereira C, Simoes PA, Celestino R, Reis RM, Barbosa DJ, Pires HR, Carvalho C, Amorim J, Carvalho AX *et al* (2017) Molecular mechanism of dynein recruitment to kinetochores by the Rod-Zw10-Zwilch complex and Spindly. *J Cell Biol* 216: 943–960

Gassmann R (2023) Dynein at the kinetochore. *J Cell Sci* 136: jcs220269

Gassmann R, Holland AJ, Varma D, Wan X, Civril F, Cleveland DW, Oegema K, Salmon ED, Desai A (2010) Removal of Spindly from microtubule-attached kinetochores controls spindle checkpoint silencing in human cells. *Genes Dev* 24: 957–971

Gibson DG, Young L, Chuang RY, Venter JC, Hutchison CA 3rd, Smith HO (2009) Enzymatic assembly of DNA molecules up to several hundred kilobases. *Nat Methods* 6: 343–345

Griffis ER, Stuurman N, Vale RD (2007) Spindly, a novel protein essential for silencing the spindle assembly checkpoint, recruits dynein to the kinetochore. *J Cell Biol* 177: 1005–1015

Hiruma Y, Sacristan C, Pachis ST, Adamopoulos A, Kuijt T, Ubbink M, von Castelmur E, Perrakis A, Kops GJ (2015) CELL DIVISION CYCLE. Competition

between MPS1 and microtubules at kinetochores regulates spindle checkpoint signaling. *Science* 348: 1264–1267

Hoffman DB, Pearson CG, Yen TJ, Howell BJ, Salmon ED (2001) Microtubule-dependent changes in assembly of microtubule motor proteins and mitotic spindle checkpoint proteins at PtK1 kinetochores. *Mol Biol Cell* 12: 1995–2009

Jackman M, Marcozzi C, Barbiero M, Pardo M, Yu L, Tyson AL, Choudhary JS, Pines J (2020) Cyclin B1-Cdk1 facilitates MAD1 release from the nuclear pore to ensure a robust spindle checkpoint. *J Cell Biol* 219: e201907082

Ji Z, Gao H, Yu H (2015) CELL DIVISION CYCLE. Kinetochore attachment sensed by competitive Mps1 and microtubule binding to Ndc80C. *Science* 348: 1260–1264

Jumper J, Evans R, Pritzel A, Green T, Figurnov M, Ronneberger O, Tunyasuvunakool K, Bates R, Zidek A, Potapenko A *et al* (2021) Highly accurate protein structure prediction with AlphaFold. *Nature* 596: 583–589

Katoh Y, Terada M, Nishijima Y, Takei R, Nozaki S, Hamada H, Nakayama K (2016) Overall architecture of the intraflagellar transport (IFT)-B complex containing Cluap1/IFT38 as an essential component of the IFT-B peripheral subcomplex. *J Biol Chem* 291: 10962–10975

Kendrick AA, Dickey AM, Redwine WB, Tran PT, Vaites LP, Dzieciatkowska M, Harper JW, Reck-Peterson SL (2019) Hook3 is a scaffold for the opposite-polarity microtubule-based motors cytoplasmic dynein-1 and KIF1C. *J Cell Biol* 218: 2982–3001

Kim Y, Heuser JE, Waterman CM, Cleveland DW (2008) CENP-E combines a slow, processive motor and a flexible coiled coil to produce an essential motile kinetochore tether. *J Cell Biol* 181: 411–419

Kim Y, Holland AJ, Lan W, Cleveland DW (2010) Aurora kinases and protein phosphatase 1 mediate chromosome congression through regulation of CENP-E. *Cell* 142: 444–455

Kops G, Gassmann R (2020) Crowning the kinetochore: the fibrous corona in chromosome segregation. *Trends Cell Biol* 30: 653–667

Krenn V, Musacchio A (2015) The Aurora B kinase in chromosome Bi-orientation and Spindle checkpoint signaling. *Front Oncol* 5: 225

Krenn V, Wehenkel A, Li X, Santaguida S, Musacchio A (2012) Structural analysis reveals features of the spindle checkpoint kinase Bub1-kinetochore subunit Knl1 interaction. *J Cell Biol* 196: 451–467

Krenn V, Overlack K, Primorac I, van Gerwen S, Musacchio A (2014) KI motifs of human Knl1 enhance assembly of comprehensive spindle checkpoint complexes around MELT repeats. *Curr Biol* 24: 29–39

Kuhn J, Dumont S (2017) Spindle assembly checkpoint satisfaction occurs via end-on but not lateral attachments under tension. *J Cell Biol* 216: 1533–1542

Kuhn J, Dumont S (2019) Mammalian kinetochores count attached microtubules in a sensitive and switch-like manner. *J Cell Biol* 218: 3583–3596

Lampson MA, Grishchuk EL (2017) Mechanisms to avoid and correct erroneous kinetochore-microtubule attachments. *Biology (Basel)* 6: 1

Lampson MA, Kapoor TM (2005) The human mitotic checkpoint protein BubR1 regulates chromosome-spindle attachments. *Nat Cell Biol* 7: 93–98

Lara-Gonzalez P, Pines J, Desai A (2021) Spindle assembly checkpoint activation and silencing at kinetochores. *Semin Cell Dev Biol* 117: 86–98

Legal T, Hayward D, Gluszek-Kustusz A, Blackburn EA, Spanos C, Rappsilber J, Gruneberg U, Welburn JPI (2020) The C-terminal helix of BubR1 is essential for CENP-E-dependent chromosome alignment. *J Cell Sci* 133: jcs246025

Lin YT, Chen Y, Wu G, Lee WH (2006) Hec1 sequentially recruits Zwint-1 and ZW10 to kinetochores for faithful chromosome segregation and spindle checkpoint control. *Oncogene* 25: 6901–6914

Liu D, Vleugel M, Backer CB, Hori T, Fukagawa T, Cheeseman IM, Lampson MA (2010) Regulated targeting of protein phosphatase 1 to the outer kinetochore by KNL1 opposes Aurora B kinase. *J Cell Biol* 188: 809–820

London N, Ceto S, Ranish JA, Biggins S (2012) Phosphoregulation of Spc105 by Mps1 and PP1 regulates Bub1 localization to kinetochores. *Curr Biol* 22: 900–906

Luo Y, Ahmad E, Liu ST (2018) MAD1: kinetochore receptors and catalytic mechanisms. *Front Cell Dev Biol* 6: 51

Magidson V, Paul R, Yang N, Ault JG, O'Connell CB, Tikhonenko I, McEwen BF, Mogilner A, Khodjakov A (2015) Adaptive changes in the kinetochore architecture facilitate proper spindle assembly. *Nat Cell Biol* 17: 1134–1144

Maldonado M, Kapoor TM (2011) Constitutive Mad1 targeting to kinetochores uncouples checkpoint signalling from chromosome biorientation. *Nat Cell Biol* 13: 475–482

Mao Y, Abrieu A, Cleveland DW (2003) Activating and silencing the mitotic checkpoint through CENP-E-dependent activation/inactivation of BubR1. *Cell* 114: 87–98

Mao Y, Desai A, Cleveland DW (2005) Microtubule capture by CENP-E silences BubR1-dependent mitotic checkpoint signaling. *J Cell Biol* 170: 873–880

Martin-Lluesma S, Stucke VM, Nigg EA (2002) Role of Hec1 in spindle checkpoint signaling and kinetochore recruitment of Mad1/Mad2. *Science* 297: 2267–2270

Meadows JC, Shepperd LA, Vanoosthuyse V, Lancaster TC, Sochaj AM, Buttrick GJ, Hardwick KG, Millar JB (2011) Spindle checkpoint silencing requires association of PP1 to both Spc7 and kinesin-8 motors. *Dev Cell* 20: 739–750

Mitevska O, Lam PW, Daly L, Auckland P (2023) Lis1-dynein drives corona compaction and limits erroneous microtubule attachment at kinetochores. *J Cell Sci* 136: jcs260226

Mosalaganti S, Keller J, Altenfeld A, Winzker M, Rombaut P, Saur M, Petrovic A, Wehenkel A, Wohlgemuth S, Muller F *et al* (2017) Structure of the RZZ complex and molecular basis of its interaction with Spindly. *J Cell Biol* 216: 961–981

Musacchio A, Desai A (2017) A molecular view of kinetochore assembly and function. *Biology (Basel)* 6: 5

Nousiainen M, Sillje HH, Sauer G, Nigg EA, Korner R (2006) Phosphoproteome analysis of the human mitotic spindle. *Proc Natl Acad Sci U S A* 103: 5391–5396

Ohashi A, Ohori M, Iwai K, Nambu T, Miyamoto M, Kawamoto T, Okaniwa M (2015) A novel time-dependent CENP-E inhibitor with potent antitumor activity. *PLoS One* 10: e0144675

Olenick MA, Holzbaur ELF (2019) Dynein activators and adaptors at a glance. *J Cell Sci* 132: jcs227132

Overlack K, Primorac I, Vleugel M, Krenn V, Maffini S, Hoffmann I, Kops GJ, Musacchio A (2015) A molecular basis for the differential roles of Bub1 and BubR1 in the spindle assembly checkpoint. *Elife* 4: e05269

Owa M, Dynlacht B (2021) A non-canonical function for Centromere-associated protein-E controls centrosome integrity and orientation of cell division. *Commun Biol* 4: 358

Pagliuca C, Draviam VM, Marco E, Sorger PK, De Wulf P (2009) Roles for the conserved spc105p/kre28p complex in kinetochore-microtubule binding and the spindle assembly checkpoint. *PLoS One* 4: e7640

Pereira C, Reis RM, Gama JB, Celestino R, Cheerambathur DK, Carvalho AX, Gassmann R (2018) Self-assembly of the RZZ complex into filaments drives kinetochore expansion in the absence of microtubule attachment. *Curr Biol* 28: 3408–3421

Pfarr CM, Coue M, Grissom PM, Hays TS, Porter ME, McIntosh JR (1990) Cytoplasmic dynein is localized to kinetochores during mitosis. *Nature* 345: 263–265

Polley S, Müschenborn H, Terbeck M, De Antoni A, Vetter IR, Dogterom M, Musacchio A, Volkov VA, Huis in 't Veld PJ (2023) Stable kinetochore-microtubule attachment requires loop-dependent Ndc80-Ndc80 binding. *EMBO J* 42: e112504

Primorac I, Weir JR, Chiroli E, Gross F, Hoffmann I, van Gerwen S, Ciliberto A, Musacchio A (2013) Bub3 reads phosphorylated MELT repeats to promote spindle assembly checkpoint signaling. *Elife* 2: e01030

Qiu R, Zhang J, Xiang X (2023) Kinesin-1 autoinhibition facilitates the initiation of dynein cargo transport. *J Cell Biol* 222: e202205136

Raisch T, Ciossani G, d'Amico E, Cmentowski V, Carmignani S, Maffini S, Merino F, Wohlgemuth S, Vetter IR, Raunser S *et al* (2022) Structure of the RZZ complex and molecular basis of Spindly-driven corona assembly at human kinetochores. *EMBO J* 41: e110411

Randall TS, Moores C, Stephenson FA (2013) Delineation of the TRAK binding regions of the kinesin-1 motor proteins. *FEBS Lett* 587: 3763–3769

Reck-Peterson SL, Redwine WB, Vale RD, Carter AP (2018) The cytoplasmic dynein transport machinery and its many cargoes. *Nat Rev Mol Cell Biol* 19: 382–398

Rodriguez-Rodriguez JA, Lewis C, McKinley KL, Sikirzhytski V, Corona J, Maciejowski J, Khodjakov A, Cheeseman IM, Jallepalli PV (2018) Distinct roles of RZZ and Bub1-KNL1 in mitotic checkpoint signaling and kinetochore expansion. *Curr Biol* 28: 3422–3429

Sacristan C, Ahmad MUD, Keller J, Fermie J, Groenewold V, Tromer E, Fish A, Melero R, Carazo JM, Klumperman J *et al* (2018) Dynamic kinetochore size regulation promotes microtubule capture and chromosome biorientation in mitosis. *Nat Cell Biol* 20: 800–810

Santaguida S, Tighe A, D'Alise AM, Taylor SS, Musacchio A (2010) Dissecting the role of MPS1 in chromosome biorientation and the spindle checkpoint through the small molecule inhibitor reversine. *J Cell Biol* 190: 73–87

Sharp-Baker H, Chen RH (2001) Spindle checkpoint protein Bub1 is required for kinetochore localization of Mad1, Mad2, Bub3, and CENP-E, independently of its kinase activity. *J Cell Biol* 153: 1239–1250

Silio V, McAinsh AD, Millar JB (2015) KNL1-bubs and RZZ provide two separable pathways for checkpoint activation at human kinetochores. *Dev Cell* 35: 600–613

Stucke VM, Baumann C, Nigg EA (2004) Kinetochore localization and microtubule interaction of the human spindle checkpoint kinase Mps1. *Chromosoma* 113: 1–15

Suijkerbuijk SJ, van Dam TJ, Karagoz GE, von Castelmur E, Hubner NC, Duarte AM, Vleugel M, Perrakis A, Rudiger SG, Snel B *et al* (2012) The vertebrate mitotic checkpoint protein BUBR1 is an unusual pseudokinase. *Dev Cell* 22: 1321–1329

Sundin LJ, Guimaraes GJ, Deluca JG (2011) The NDC80 complex proteins Nuf2 and Hec1 make distinct contributions to kinetochore-microtubule attachment in mitosis. *Mol Biol Cell* 22: 759–768

Thrower DA, Jordan MA, Schaar BT, Yen TJ, Wilson L (1995) Mitotic HeLa cells contain a CENP-E-associated minus end-directed microtubule motor. *EMBO J* 14: 918–926

Varma D, Wan X, Cheerambathur D, Gassmann R, Suzuki A, Lawrimore J, Desai A, Salmon ED (2013) Spindle assembly checkpoint proteins are positioned close to core microtubule attachment sites at kinetochores. *J Cell Biol* 202: 735–746

Vergnolle MA, Taylor SS (2007) Cenp-F links kinetochores to Ndel1/Nde1/Lis1/dynein microtubule motor complexes. *Curr Biol* 17: 1173–1179

Vitre B, Gudimchuk N, Borda R, Kim Y, Heuser JE, Cleveland DW, Grishchuk EL (2014) Kinetochore-microtubule attachment throughout mitosis potentiated by the elongated stalk of the kinetochore kinesin CENP-E. *Mol Biol Cell* 25: 2272–2281

Vleugel M, Tromer E, Omerzu M, Groenewold V, Nijenhuis W, Snel B, Kops GJ (2013) Arrayed BUB recruitment modules in the kinetochore scaffold KNL1 promote accurate chromosome segregation. *J Cell Biol* 203: 943–955

Weissmann F, Petzold G, VanderLinden R, Huis In 't Veld PJ, Brown NG, Lampert F, Westermann S, Stark H, Schulman BA, Peters JM (2016) biGBac enables rapid gene assembly for the expression of large multisubunit protein complexes. *Proc Natl Acad Sci U S A* 113: E2564–E2569

Wojcik E, Basto R, Serr M, Scaerou F, Karess R, Hays T (2001) Kinetochore dynein: its dynamics and role in the transport of the rough deal checkpoint protein. *Nat Cell Biol* 3: 1001–1007

Wood KW, Lad L, Luo L, Qian X, Knight SD, Nevins N, Brejc K, Sutton D, Gilmartin AG, Chua PR *et al* (2010) Antitumor activity of an allosteric inhibitor of centromere-associated protein-E. *Proc Natl Acad Sci U S A* 107: 5839–5844

Wu J, Larreategui-Aparicio A, Lambers MLA, Bodor DL, Klaasen SJ, Tollenaar E, de Ruijter-Villani M, Kops G (2023) Microtubule nucleation from the fibrous corona by LIC1-pericentrin promotes chromosome congression. *Curr Biol* 33: 912–925

Yamagishi Y, Yang CH, Tanno Y, Watanabe Y (2012) MPS1/Mph1 phosphorylates the kinetochore protein KNL1/Spc7 to recruit SAC components. *Nat Cell Biol* 14: 746–752

Yamamoto TG, Watanabe S, Essex A, Kitagawa R (2008) SPDL-1 functions as a kinetochore receptor for MDF-1 in *Caenorhabditis elegans*. *J Cell Biol* 183: 187–194

Yao X, Anderson KL, Cleveland DW (1997) The microtubule-dependent motor centromere-associated protein E (CENP-E) is an integral component of kinetochore corona fibers that link centromeres to spindle microtubules. *J Cell Biol* 139: 435–447

Yao X, Abrieu A, Zheng Y, Sullivan KF, Cleveland DW (2000) CENP-E forms a link between attachment of spindle microtubules to kinetochores and the mitotic checkpoint. *Nat Cell Biol* 2: 484–491

Yen TJ, Compton DA, Wise D, Zinkowski RP, Brinkley BR, Earnshaw WC, Cleveland DW (1991) CENP-E, a novel human centromere-associated protein required for progression from metaphase to anaphase. *EMBO J* 10: 1245–1254

Yen TJ, Li G, Schaar BT, Szilak I, Cleveland DW (1992) CENP-E is a putative kinetochore motor that accumulates just before mitosis. *Nature* 359: 536–539